UNIVERSIDAD DE CONCEPCIÓN
FACULTAD DE CIENCIAS FÍSICAS Y MATEMÁTICAS

THERMODYNAMICS OF MAGNETIZED BPS BARYONIC LAYERS AND THE EFFECTS OF THE ISOSPIN CHEMICAL POTENTIAL

Por: Evangelo Exequiel Delgado Yáñez

Tesis presentada a la Facultad de Ciencias Físicas y Matemáticas de la Universidad de Concepción para optar al grado académico de Magíster en Ciencias con Mención en Física

Marzo 2026

Concepción, Chile

Profesor Guía: Dr. Fabrizio Canfora Tartaglia

A mis Padres y Hermanos

Agradecimientos

Quiero dedicar esta sección a agradecer a todas las personas que, de una u otra forma, me acompañaron durante este proceso. Sé que resulta imposible plasmar en un par de páginas la infinita gratitud que siento, pero haré mi mejor esfuerzo.

En primer lugar, quiero agradecer a mi guía de tesis, el Dr. Fabrizio Canfora, por su paciencia y confianza en mí, por enseñarme que hacer ciencia es un arte que requiere disciplina y esfuerzo constante, y que incluso en lo más pequeño uno puede encontrar un mundo de investigación fascinante. También agradezco al Dr. Julio Oliva, quien me motivó a interesarme en el área de la física de altas energías con sus cursos y carisma, por enseñarme los aspectos más fundamentales de la física y por su apoyo y confianza durante mis últimos años de formación. Finalmente, agradezco al Dr. Andrés Anabalón por su apoyo durante mi primer año de magíster y por enseñarme a profundizar en las ideas de las teorías de la física y a ver más allá. Y a todas las profesoras y profesores que pasaron por mi formación.

Quiero agradecer a mi familia, a mis padres Valentina Yáñez y Eduardo Delgado, quienes me inculcaron desde muy pequeño la curiosidad por los fenómenos naturales y por el mundo que nos rodea, por enseñarme a jamás rendirme y a luchar siempre por lo que quiero, y por darme las herramientas para seguir adelante. Les agradezco, sobre todo, su amor incondicional, porque es gracias a ustedes que soy la persona que soy hoy en día. Agradezco a mis hermanos Rafaela, Jose Joaquín y Anapaula por ese amor de hermanos que demostramos de forma silenciosa, por acompañarnos en los momentos difíciles, por intentar siempre sacarnos una sonrisa y por su apoyo incondicional. También agradezco a los peludos del hogar, Boni, Pilchard y Marcel, que con su inocencia y cariño animal alegran la vida en casa.

A mis tías, Carol Yáñez y María Ester Delgado, les agradezco su guía, amor y cariño, por asegurarse de estar siempre presentes para nosotros y por cuidarnos a mí y a mis hermanos como si fuésemos sus hijos. A mi prima Catalina Rozas, por su cariño y preocupación, por ser un ejemplo a seguir para mi y mis hermanos.

A mi abuelita, María Pincheira, quien partió antes de poder verme llegar hasta

acá, le agradezco su infinito amor, su sabiduría de campo y por darme todo el cariño que un niño sensible necesitaba. Sé que me cuida desde algún lado y sé que estaría orgullosa de la persona que soy.

También me gustaría agradecer a mis amigos, quienes me han acompañado durante estos años. A José Garrido, con quien nos conocemos desde los 10 años, le agradezco los consejos, las conversaciones, las risas y por crecer juntos. Agradezco a Franco Ramírez por su compañía, su visión tan única de la vida y por acercarme a la música. A Michelle Valdés, quien fue muy importante durante mi primer semestre de universidad, le agradezco las conversaciones y reflexiones, especialmente por su compañía durante la pandemia y por estar siempre, a pesar de la distancia.

Obviamente, no puedo dejar de lado a mis amigos y compañeros de universidad, con quienes hemos recorrido todo este camino. En primer lugar, quiero agradecer a Enrique Orellana, Leonardo Gajardo, Juan Illanes y Lorena Sepúlveda, quienes son un pilar fundamental en mi formación. Agradezco todo lo que he aprendido de ustedes, las salidas, las tardes estudiando, su compañía y su amistad, gracias por hacer la vida universitaria más amena. Agradezco a José Rosas por las conversaciones y discusiones sobre la filosofía de la física y por las tardes tocando música. También agradezco a Luis Urrutia y Alejandro Saavedra, a quienes considero mis hermanos mayores académicos, por todo lo que me han enseñado. Finalmente, quiero agradecer a Karla Rodríguez, Benjamín Mellado, Aníbal Neira, Agustín Cáceres, Nicolás Águila, Lucas Sanhueza y Camilo Jordán, con quienes he podido compartir estos últimos años de carrera y que se han convertido en un apoyo fundamental.

Como decía Juan Bosco: “un colegio sin música es un cuerpo sin alma”. Quiero agradecer al Coro Sinfónico de la Universidad de Concepción por brindarme el espacio para desarrollar el canto y la oportunidad de participar en obras maravillosas del repertorio operístico y de la música coral. Agradezco también a todas las personas que conocí allí, por su calidez y compañía.

Finalmente, quiero agradecer a mi más importante compañía durante estos años, mi pareja Cielo Ramírez de Arellano, gracias por confiar en mí y apoyarme. Agradezco tu amor genuino y tu calidez, por darme un espacio en donde poder sentirme seguro y descansar. Gracias por todo lo que hemos construido, por nuestro cariño, nuestro humor, nuestra confianza, por esta relación tan sana que

hemos cultivado. Gracias por creer en mí.

Este trabajo ha sido realizado gracias al proyecto FONDECYT Regular Grant 1240048.

Resumen

Estudiamos la termodinámica de capas bariónicas BPS magnetizadas, las cuales poseen tanto carga bariónica como flujo magnético. El estudio termodinámico de este sistema resulta altamente no trivial debido a que la carga topológica, que aparece naturalmente en el lado derecho de la cota BPS, es una función no lineal de la carga bariónica. Estas capas fueron construidas a través de la ecuación de Hamilton-Jacobi de la mecánica clásica en el modelo sigma no lineal acoplado minimalmente a la teoría de Maxwell, la cual es una de las teorías efectivas más relevantes para la cromodinámica cuántica (QCD) en el régimen fuertemente interactuante del límite de bajas energías que también toma en consideración las interacciones electromagnéticas. Para la construcción de la función de partición grancanónica del sistema (que resulta interesante por su relación con la función zeta de Riemann), utilizamos herramientas del efecto Casimir para derivar una relación analítica entre la carga topológica, la carga bariónica y el flujo magnético. Con base en esto y utilizando física estadística clásica, fue posible derivar cantidades termodinámicas relevantes de estas capas, tales como la energía, la entropía, la capacidad calorífica y la susceptibilidad magnética, logrando identificar el potencial químico bariónico crítico. Los efectos del potencial químico de isospín también pueden ser incluidos: en particular, construimos una cota BPS explícita y las correspondientes configuraciones BPS para el caso en el que el potencial químico de isospín es no nulo. Por otro lado, derivamos de forma analítica, a partir del tensor de energía momento del sistema, la ecuación de estado y la velocidad del sonido tanto para el caso con potencial químico de isospín cero como distinto de cero. Desde el punto de vista técnico, es un resultado bastante notable derivar expresiones explícitas para todas estas cantidades termodinámicas de un sistema magnetizado fuertemente interactuante a densidad bariónica finita. Finalmente, la interpretación física de nuestros resultados analíticos será discutida.

Keywords – Termodinámica, Modelo sigma no lineal, Cota BPS, Capas bariónicas, Potencial químico de isospín, Ecuación de estado, Efecto casimir

Abstract

We study the thermodynamics of magnetized BPS baryonic layers, which possess both baryonic charge and magnetic flux. The thermodynamic study of this interacting system is highly non-trivial because the topological charge, which naturally appears on the right-hand side of the BPS bound, is a non-linear function of the baryonic charge. These layers were constructed using the Hamilton-Jacobi equation of classical mechanics in the non-linear sigma model minimally coupled to Maxwell's theory, which is one of the most relevant effective theories for Quantum Chromodynamics (QCD) in the strongly interacting regime of the low-energy limit, which also takes electromagnetic interactions into account. To construct the grand canonical partition function of the system (which is interestingly related to the Riemann zeta function), we used tools from the Casimir effect to derive an analytical relationship between the topological charge, the baryonic charge, and the magnetic flux. Based on this, and using classical statistical physics, it was possible to derive relevant thermodynamic quantities of these layers, such as energy, entropy, heat capacity, and magnetic susceptibility, successfully identifying the critical baryonic chemical potential. The effects of the isospin chemical potential can also be included: in particular, we constructed an explicit BPS bound and the corresponding BPS configurations for the case in which the isospin chemical potential is non-zero. Furthermore, we analytically derived, from the energy-momentum tensor of the system, the equation of state and the speed of sound for both the cases with zero and non-zero isospin chemical potential. From a technical point of view, it is a quite remarkable result to derive explicit expressions for all these thermodynamic quantities of a strongly interacting magnetized system at finite baryonic density. Finally, the physical interpretation of our analytical results will be discussed.

Keywords – Thermodynamics, Non-linear sigma model, BPS bound, Baryonic layers, Isospin chemical potential, Equation of state, Casimir effect

Contents

List of Figures

Chapter 1

Introduction

The study of nuclear matter under extreme conditions, such as finite density, low temperatures, and external magnetic fields, is one of the most significant open problems in modern theoretical physics. This is largely motivated by the consideration of astrophysical environments in which these conditions occur, such as the interior of neutron stars or in heavy-ion collisions [1, 2, 3, 4, 5, 6, 7, 8, 9, 10, 11, 12, 13]. In these scenarios, nuclear matter is expected to form ordered patterns, these non-homogeneous condensates are known as nuclear pasta phases [14, 15, 16, 17, 8, 18, 19, 20, 21, 9, 22, 10, 23, 24, 25]. These structures can take different forms such as tubes (spaghetti) or layers (lasagna); we will be particularly interested in the latter.

Quantum chromodynamics (QCD), as the field theory describing the strong interaction, should be able to describe these phases. However, in the low-energy regime with finite baryonic density, which characterizes these systems, we face several difficulties. First, the QCD coupling constant increases as the energy decreases (and vice versa), making it impossible to use perturbation theory in this region. On the other hand, computational methods such as lattice QCD are severely limited by the well known sign problem [26, 27, 28, 29]. Because of these difficulties, it is essential to search for effective models that capture the essence of QCD and allow for an analytical treatment.

In this context, the Skyrme model has proven to be an excellent tool for this purpose. In the low-energy limit of QCD, baryons emerge as topological solitons (skyrmions) in a mesonic field theory [30, 31, 32, 33, 34, 35]. There is compelling

evidence connecting the properties of baryons with those of these skyrmions, which justifies the use of this type of model to describe hadronic structure. Following this line of research, recent works have proposed ansatz that allow one to obtain exact analytical solutions corresponding to hadronic matter distributed in tubes and layers configurations [36, 37, 38, 39, 40, 41, 42, 43, 44, 45, 46, 47, 48, 49, 50, 51, 52, 53, 54]. Nevertheless, the construction of purely magnetic configurations, which are of great astrophysical relevance, had remained elusive until recently.

The main objective of this thesis is precisely to address this gap by providing a concrete and analytically tractable example of a strongly interacting system with finite baryon charge, similar to the lasagna-type phase of nuclear pasta. To this end, we focus on the study of magnetized baryonic layers. Unlike previous works that included coupled electric and magnetic fields, here we succeed in constructing purely magnetic configurations thanks to a technique based on the Hamilton–Jacobi equation of classical mechanics. This formalism allows us to derive a nontrivial BPS (Bogomol'nyi–Prasad–Sommerfield) bound for the nonlinear sigma model with global $SU(2)$ symmetry, minimally coupled to Maxwell theory (G-NLSM) [55, 56, 57, 58]. Although in this thesis we do not use the full Skyrme model, the Hamilton–Jacobi technique can be extended to include the Skyrme term. This extension will be part of future work.

It is important to emphasize that, although the full Skyrme model requires a fourth-order term (the Skyrme term) to stabilize the solutions in a finite space [59], our solutions are defined in a fixed finite spatial volume. This condition, following Derrick's theorem, circumvents the need for such a term, allowing us to work with the G-NLSM and drastically simplifying the analysis.

The BPS nature of our solutions is fundamental for the study of thermodynamics. Thanks to it, we can establish an analytical relation between the topological charge, the baryon charge, and the magnetic flux of these configurations. A crucial step in this process is the determination of the "chemical potential" for the magnetic flux, denoted by I_0, which arises as an integration constant in the Hamilton–Jacobi equations. Although it is not possible to obtain a closed analytical expression for I_0, in this work, using tools from Casimir effect theory, it was possible to find an analytical approximation for this quantity. This calculation is essential for constructing the grand canonical partition function of the system, and from it deriving its fundamental thermodynamic properties, such as the internal energy,

entropy, heat capacity, and magnetic susceptibility. Moreover, from the energy-momentum tensor of the configurations, we have been able to derive the equation of state and the speed of sound.

Finally, a natural question is whether this analysis can be extended to more realistic conditions. In particular, the inclusion of the isospin chemical potential is essential for a more complete description of these magnetized baryonic layers. Far from destroying the BPS property, we will show that the presence of this chemical potential modifies it in an elegant and manageable way. As will be seen, its effects can be interpreted as a dressing or modification of the coupling constants of the system. Notably, the analysis of the energy-momentum tensor extends naturally to the isospin case, allowing us to obtain the equation of state and the speed of sound also in the presence of this potential, which reinforces the completeness of our thermodynamic study. For the sake of clarity, we will first develop the formalism for the case without isospin chemical potential and subsequently introduce its effects in order to construct the isospin-dependent BPS magnetized baryonic layers.

This thesis is organized as follows: in chapter 2, we present the G-NLSM. Chapter 3 is devoted to the ansatz for the construction of magnetized Baryonic layers, the corresponding BPS bound, the topological charge and its relation to the magnetic flux, as well as a discussion on the boundary conditions for $H(r)$ and finally we introduce a couple of approximations for the integration constant I_0. The grand canonical partition function is constructed in chapter 4, where we also compute several relevant thermodynamical quantities, we also construct the equation of state and derive the speed of sound, and we explore the contribution of an external magnetic field to the energy and compute the magnetic susceptibility. In chapter 5, the effects of the Isospin chemical potential will be included, and we will construct the BPS bound and the corresponding BPS configurations in the case in which the Isospin chemical potential is non-zero. Chapter 6 contains some comments and concluding remarks.

This thesis is based on the results presented in [60], of which the author is a co-author. The figures presented throughout this manuscript correspond to the original plots from that work and are included here using the original source files, rather than independent reproductions.

Chapter 2

The Non-Linear Sigma Model

In this chapter, we introduce the framework of our study: the Non-linear Sigma Model (NLSM). As an effective field theory, the NLSM provides a robust description of the low-energy dynamics of Quantum Chromodynamics (QCD), a regime where standard perturbation theory fails due to color confinement. First, in section 2.1, we discuss the gauged version of the NLSM, introducing the coupling with the Maxwell theory to account for electromagnetic interactions. Then, in section 2.2, we construct and analyze exact solutions representing magnetized BPS baryonic layers. These solutions are of great physical interest as they serve as a theoretical baseline for understanding ordered hadronic structures under the influence of magnetic fields.

2.1 Gauged Non-Linear Sigma Model

To describe the low-energy limit of QCD, we consider the nonlinear sigma model minimally coupled to Maxwell theory in $(3+1)$ dimensions with global $SU(2)$ symmetry, whose action is given by

$$S = -\frac{1}{4}\int d^4x \left\{K\mathrm{Tr}\{\Sigma^\mu\Sigma_\mu\} - F_{\mu\nu}F^{\mu\nu}\right\}, \tag{2.1.1}$$

where $K = \frac{f_\pi^2}{4}$ is the coupling constant of the G-NLSM and f_π is the pion decay constant [61], whose numerical values will be discussed later in chapter 4. A mass term for the pions could also be included, however the mass of the baryonic layers is many orders of magnitude larger than the pion mass, so that the mass term can

be safely neglected. The indices $\mu, \nu = 0, 1, 2, 3$ denotes spacetime indices, where 0 corresponds to the timelike component. Moreover,

$$\Sigma_\mu = U^{-1} D_\mu U, \quad F_{\mu\nu} = \partial_\mu A_\nu - \partial_\nu A_\mu, \tag{2.1.2}$$

where A_μ represents the $U(1)$ gauge field and U is a scalar field taking values in $SU(2)$, defined as a map

$$U : \mathbb{R}^3 \to SU(2). \tag{2.1.3}$$

In the following sections, the $SU(2)$ valued U field will be parametrized using generalized Euler angles [62, 63, 64], since every element of $SU(2)$ admits a unique representation in this parametrization,

$$U = e^{\tau_3 F} e^{\tau_2 H} e^{\tau_3 G}. \tag{2.1.4}$$

Here $F(x^\mu)$, $H(x^\mu)$ and $G(x^\mu)$ represent the three scalar degrees of freedom of the $SU(2)$ field

$$F, G, H : \mathbb{R}^{3+1} \mapsto \mathbb{R}. \tag{2.1.5}$$

As already shown, for instance, in [52], this parameterization leads to configurations in which baryons are organized in layers.

The covariant derivative introduced in (2.1.2) is defined as

$$D_\mu U = \partial_\mu U + A_\mu [\tau_3, U], \tag{2.1.6}$$

where τ_j are defined as $\tau_j = i\sigma_j$, with σ_j the Pauli matrices.

By varying the action with respect to the fundamental fields, the equations of motion of the model are obtained as

$$D_\mu \Sigma^\mu = 0, \tag{2.1.7}$$

$$\partial_\mu F^{\mu\nu} = J^\nu, \tag{2.1.8}$$

where the conserved current J^μ is given by

$$J^\mu = \frac{K}{2} \mathrm{Tr} \left\{ \hat{O}_3 \Sigma^\mu \right\}, \quad \hat{O}_3 = U^{-1} \tau_3 U - \tau_3. \tag{2.1.9}$$

Furthermore, the energy-momentum tensor for the G-NLSM is

$$T_{\mu\nu} = -\frac{K}{2}\mathrm{Tr}\left\{\Sigma_\mu\Sigma_\nu - \frac{1}{2}g_{\mu\nu}\Sigma^\alpha\Sigma_\alpha\right\} + \bar{T}_{\mu\nu}, \tag{2.1.10}$$

such that $\bar{T}_{\mu\nu}$ is the energy–momentum tensor associated with the electromagnetic interaction, given by

$$\bar{T}_{\mu\nu} = -F_{\mu\alpha}F^\alpha_\nu + \frac{1}{4}F_{\alpha\beta}F^{\alpha\beta}g_{\mu\nu}. \tag{2.1.11}$$

Different solutions of the equations of motion are classified by a topological invariant, which we denote by B, defined as the index of the map U, namely $B = \mathrm{index}(U)$. This index takes integer values and is directly associated with the number of baryons in the system, which we will refer to as the baryonic charge [59], and which can be computed explicitly as follows

$$B = \frac{1}{24\pi^4}\int_V \rho_B, \tag{2.1.12}$$

where V is the volume of the system and ρ_B defined as

$$\rho_B = \rho_{B_1} + \rho_{B_2} \tag{2.1.13}$$

represents the baryonic density (see [53] and references therein), where

$$\rho_{B_1} = \varepsilon^{ijk}\mathrm{Tr}\left\{(U^{-1}\partial_i U)(U^{-1}\partial_j U)(U^{-1}\partial_k U)\right\}, \tag{2.1.14}$$

$$\rho_{B_2} = -3\varepsilon^{ijk}\mathrm{Tr}\left\{\partial_i\left[A_j\tau_3(U^{-1}\partial_k U + \partial_k U U^{-1})\right]\right\}. \tag{2.1.15}$$

Therefore, the quantities defined in (2.1.12), (2.1.13), (2.1.14) and (2.1.15) are both topological invariants and gauge invariant quantities.

2.2 Magnetized BPS baryonic layers

As stated in the previous section, the choice of a suitable ansatz is crucial for obtaining analytic solutions to the field equations. In this section, we will study an ansatz that yields static purely magnetic solutions in the BPS limit.

To this end, we explicitly compute the quantities introduced in the previous section using the Euler-angle parametrization (2.1.4). Since we aim to study the emergence of topologically nontrivial inhomogeneous condensates at finite density and finite volume, the simplest way to incorporate this into the calculations is to introduce the following flat metric

$$ds^2 = -dt^2 + L^2(dx^2 + dy^2) + L_r^2 dr^2 \tag{2.2.1}$$

where x, y and r are dimensionless Cartesian coordinates that have ranges

$$0 \leq x \leq \pi, \quad 0 \leq y \leq 2\pi, \quad 0 \leq r \leq 2\pi. \tag{2.2.2}$$

The dimensionality of the space is encoded in L and L_r. A more detailed discussion of the units of measure and their specific values will be given later in 4.1. This metric describes a box of volume $V = 4\pi^3 L_r L^2$, where the gauged solitons live. The area of the layer is given by $A = 2\pi^2 L^2$. It is important to note that the coordinates x and y are tangential to the layer, while the coordinate r is orthogonal (see [52, 51, 53]). As a consequence, both the energy density and baryonic density depend only on the coordinate r.

Let us consider the following static ansatz for the $SU(2)$ valued scalar field U and for the $U(1)$ gauge field A_μ

$$U = e^{py\tau_3} e^{H(r)\tau_2} e^{px\tau_3}, \tag{2.2.3}$$

$$A_\mu = \left(0, 0, \frac{p}{2} - u(r), -\frac{p}{2} + u(r)\right), \tag{2.2.4}$$

where p must be an integer according to the theory of Euler angle parametrization for $SU(2)$ (see [62, 63, 64]). As shown in [43, 39, 40], with this ansatz, the seven coupled field equations reduce to two

$$H'' + 4\left(\frac{L_r}{L}\right)^2 \sin(2H)\left(\left(\frac{p}{2}\right)^2 - u^2\right) = 0, \tag{2.2.5}$$

$$u'' - 4KL_r^2 \sin^2(H) u = 0, \tag{2.2.6}$$

with the following energy density:

$$T_{00} = \frac{K}{L^2}\left[p^2\cos^2(H) + 4\sin^2(H)u^2\right] + \frac{K(H')^2}{2L_r^2} + \frac{(u')^2}{(L_r L)^2} \tag{2.2.7}$$

and baryonic density

$$\rho_B = -12p\frac{d}{dr}[u(1+\cos(2H))]. \tag{2.2.8}$$

Since the baryonic density (2.2.8) is a total derivative, the baryonic charge depends only on the boundary values of H and u, as expected. The choice of these boundary conditions will be discussed later in 3.5. It is worth mentioning that, since the configurations of interest are static and purely magnetic, the field equations are obtained by minimizing the energy, which is equivalent to treating the energy density as a Lagrangian. When the isospin chemical potential is included in the calculations, the free energy must be minimized.

Chapter 3

The BPS Bound

In this chapter, we address the mathematical and physical simplifications provided by the Bogomol'nyi-Prasad-Sommerfield (BPS) bound. Finding exact solutions to highly non-linear field equations is notoriously difficult; however, saturating a BPS bound allows us to reduce second-order differential equations to first-order ones, guaranteeing the stability of the solitonic configurations. The development of this chapter, particularly the derivation of the BPS bound and the application of the Hamilton-Jacobi equation strategy (sections 3.2 to 3.5), is strongly based on the methods and results presented in [55].First, we discuss BPS solitons in field theory 3.1. Then, in section 3.2, we introduce a novel Hamilton-Jacobi equation strategy to systematically derive these bounds. Then, in section 3.3, we apply this powerful mathematical tool to our specific case of magnetized BPS baryonic layers. Afterwards, in sections 3.4 and 3.5, we study the relationship between the topological charge, the magnetic field, and the boundary conditions on the profile $H(r)$, providing a clear physical meaning to the baryonic charge. Finally, in section 3.6, we discuss a useful approximation scheme for these configurations.

3.1 BPS solitons in field theory

On the framework of classical field theory, BPS solitons are defined as localized, stable, and finite-energy solutions of nonlinear equations of motion. As explained in [65], these non-dissipative configurations are of great importance since they allow one to explore the non-perturbative regime of various physical theories, behaving in some respects as classical extended particles.

Within the wide variety of soliton solutions, BPS (Bogomol'nyi–Prasad–Sommerfield) solitons are of great interest. These configurations emerge in theories where the energy of the system possesses a lower bound given by a topological invariant charge, known as the BPS bound. When a configuration saturates this bound, the second-order equations of motion reduce to first-order equations (BPS equations).

One of the most important features of the BPS equations is not only that they reduce the order of the equations, but also that they open a range of exact mathematical and analytical tools, even in cases where it is not possible to find closed solutions. An example where these BPS solitons appear is type II superconductors (described by the Abelian Higgs model). Although in this theory the BPS equations do not have analytical solutions, it is still possible to study various properties given the BPS configuration. Without knowing the exact analytical solutions, we can understand the dynamics of multiple vortices and calculate how many fermions can be trapped in the core of a vortex.

From a pedagogical point of view, the most elementary case of BPS solitons is the kink in $(1+1)$ dimensions, which provides a toy model to understand the saturation of the energy bound and topological stability in one spatial dimension. One step further are the vortices in $(2+1)$ dimensions, which exhibit vanishing interactions in the BPS limit and allow us to study configurations classified by a topological winding number.

It is precisely this mathematical tractability, combined with the topological stability inherent to the saturation of the BPS bound, that makes this formalism an indispensable tool. In the context of this work, we will use this formalism to model magnetized baryonic layers using a technique based on the Hamilton–Jacobi equation of classical mechanics to find a BPS bound for the G-NLSM and its corresponding BPS configurations.

3.2 Hamilton-Jacobi equation strategy

Consider the positive definite energy density T_{00} of a static system involving two interacting degrees of freedom, J_1 and J_2. In the present case, J_1 and J_2 are

related to H and u and are functions of a single spatial coordinate r:

$$T_{00} = \frac{(\partial_r J_1)^2}{2} + \frac{(\partial_r J_2)^2}{2} + V(J_1, J_2). \tag{3.2.1}$$

In this context, $V(J_1, J_2)$ represents the interaction term between the two degrees of freedom. Since the configuration is assumed to be static, the field equations for J_1 and J_2 can be obtained by treating T_{00} as the action density. To establish a BPS bound for these fields, we introduce two auxiliary quantities, Γ_1 and Γ_2, to be added to the gradients of J_1 and J_2 according to the following properties:

$$\frac{(\partial_r J_1 \pm \Gamma_1)^2}{2} + \frac{(\partial_r J_2 \pm \Gamma_2)^2}{2} = T_{00} + (\text{total derivative}). \tag{3.2.2}$$

This requirement leads to two conditions. First, the auxiliary functions must satisfy

$$\frac{(\Gamma_1)^2}{2} + \frac{(\Gamma_2)^2}{2} = V(J_1, J_2). \tag{3.2.3}$$

Second, the mixed term must be expressible as a total derivative with respect to r,

$$\Gamma_1 \partial_r J_1 + \Gamma_2 \partial_r J_2 = \text{total derivative}. \tag{3.2.4}$$

To fulfill the second condition, it is necessary to assume the existence of a function W such that

$$\Gamma_1 = \frac{\partial W}{\partial J_1}, \quad \Gamma_2 = \frac{\partial W}{\partial J_2}, \quad W = W(J_1, J_2). \tag{3.2.5}$$

With this choice, the mixed term becomes

$$\Gamma_1 \partial_r J_1 + \Gamma_2 \partial_r J_2 = \partial_r (W(J_1, J_2)). \tag{3.2.6}$$

Combining these results with the first condition yields a non-linear partial differential equation for the function W,

$$\left(\frac{\partial W}{\partial J_1}\right)^2 + \left(\frac{\partial W}{\partial J_2}\right)^2 = 2V(J_1, J_2) \implies \tag{3.2.7}$$

$$\text{total derivative} = \partial_r W, \tag{3.2.8}$$

which is precisely the form of a Hamilton-Jacobi equation for the function W, with the interaction potential V playing the role of an effective potential.

If this Hamilton-Jacobi equation admits a solution, the energy density can be expressed as a sum of squares plus a total derivative, leading to a lower bound on the total energy,

$$E \geq |W(2\pi) - W(0)|. \tag{3.2.9}$$

This bound is saturated when the fields satisfy the first order equations

$$\partial_r J_k \pm \frac{\partial W}{\partial J_k} = 0, \quad k = 1, 2. \tag{3.2.10}$$

which define the corresponding BPS configurations.

3.3 Application: magnetized BPS baryonic layers

With the technique described in the previous section, and with the following definitions:

$$\Gamma_1 = \frac{L_r}{\sqrt{K}} \frac{\partial W}{\partial H}, \quad \Gamma_2 = \frac{L_r L}{\sqrt{2}} \frac{\partial W}{\partial u}, \tag{3.3.1}$$

the Hamilton-Jacobi equation associated to the energy-density (2.2.7), is given by,

$$\frac{L_r^2}{2K} \left(\frac{\partial W}{\partial H}\right)^2 + \left(\frac{L_r L}{2}\right)^2 \left(\frac{\partial W}{\partial u}\right)^2 = \frac{K}{L^2} \left[p^2 \cos^2 H + 4u^2 \sin^2 H\right]. \tag{3.3.2}$$

This Hamilton-Jacobi equation has an analytical solution if we impose the following relations,

$$L = \frac{p}{\sqrt{2K}} \leftrightarrow A = \frac{\pi^2 p^2}{K} \leftrightarrow A = \left(\frac{2\pi p}{e f_\pi}\right)^2 \tag{3.3.3}$$

where we have explicitly written the quantization condition in terms of the pion decay constant f_π. In consequence, the BPS bound (whose definition is presented later) is saturated when the surface area of the layers is quantized according to that constant. Once this condition is satisfied, the solution of the Hamilton-Jacobi equation (3.3.2) turns out to be

$$W = \frac{4K^{\frac{3}{2}}}{pL_r} u \cos H \implies \tag{3.3.4}$$

$$\frac{\partial W}{\partial H} = \frac{4K^{\frac{3}{2}}}{pL_r} u \sin H, \quad \frac{\partial W}{\partial u} = \frac{4K^{\frac{3}{2}}}{pL_r} \cos H. \tag{3.3.5}$$

The solution of the Hamilton–Jacobi equation that we have just found, associated with the G-NLSM, allows us to write the energy density in a BPS like form as

follows:

$$T_{00} = \frac{1}{e^2}\left\{\frac{K}{2(pL_r)^2}\left[\left(pH' \pm 4\sqrt{K}L_r u \sin H\right)^2 + 4\left(u' \mp p\sqrt{K}L_r \cos H\right)^2 \pm \frac{dW}{dr}\right]\right\}, \tag{3.3.6}$$

where W is the solution of the Hamilton-Jacobi equation. From here we will only consider the upper sign in the BPS like energy-density (3.3.6). In this way, we can find the following bound for the energy:

$$E = \int d^3x\sqrt{-g}T_{00} = AL_r\int_0^{2\pi} drT_{00} \geq |Q|, \quad Q = \frac{AL_r}{e^2}|W(2\pi) - W(0)|, \tag{3.3.7}$$

where the area of the baryonic layer A is quantized according to (3.3.3).

The first order BPS equations, which imply the second order equations (2.2.5) and (2.2.6) (this follows by differentiating with respect to r), are:

$$H' + \frac{4\sqrt{K}L_r}{p}u\sin H = 0 \tag{3.3.8}$$

$$u' - p\sqrt{K}L_r\cos H = 0. \tag{3.3.9}$$

It is important to note, in order to simplify future calculations, that if we divide equation (3.3.9) by p, we find that the quantity $u(r)/p$ does not depend on p. For this reason, we define

$$v(r) \equiv \frac{u(r)}{p} \tag{3.3.10}$$

which is p-independent.

By using the BPS conditions (3.3.8) and (3.3.9), one can find an analytic relation between the gauge field v and the $SU(2)$ profile H, given by the following equation:

$$\frac{dH}{dv} = -\frac{4}{p^2}v\tan H \implies \tag{3.3.11}$$

$$H(r) = \arcsin\left[\exp\left(-2v^2(r) - I_0\right)\right], \tag{3.3.12}$$

where I_0 is an integration constant. This solution, together with the BPS equations (3.3.8) and (3.3.9), identically satisfies the field equations 2.2.5 and (2.2.6). In this way, the complete set of field equations is reduced to the following quadrature

by using (3.3.12)

$$v' = \sqrt{K} L_r \sqrt{1 - \exp\left(-4v^2(r) - 2I_0\right)}. \tag{3.3.13}$$

By integrating the equation (3.3.13), we obtain

$$2\pi = \frac{1}{\sqrt{K} L_r} \int_0^{v(2\pi)} \frac{d\tau}{\sqrt{1 - \exp(-4\tau^2 - 2I_0)}}, \tag{3.3.14}$$

where $\tau = v(r)$. Here, for convenience, we choose $v(0) = 0$. On the other hand, for the physical analysis of $v(2\pi)$, we must compute the magnetic flux in the y-direction:

$$\Phi = L L_r \int dr dx F_{rx} = \frac{p^2 \pi L_r}{\sqrt{2K}} (v(2\pi) - v(0)), \tag{3.3.15}$$

which implies that $v(2\pi)$ is proportional to the total magnetic flux in the y direction,

$$v(2\pi) = \frac{\sqrt{2K}}{p^2 \pi L_r} \Phi. \tag{3.3.16}$$

3.4 Topological charge and magnetic field

In order to construct the grand canonical partition function of the system, we must first determine explicitly both the baryonic charge (particle number) and the energy (topological charge) of the system at the BPS point. To this end, let us now consider the baryonic charge (2.1.12) with the baryonic density (2.2.8). Using the solution of H defined in (3.3.12), it takes the explicit form

$$\begin{aligned} B &= \frac{1}{24\pi^2} \int \rho_B \implies \\ |B| &= 4 \frac{\sqrt{2K}\Phi}{\pi L_r} \left(1 - \exp\left(-\frac{8K\Phi^2}{p^4 (\pi L_r)^2} - 2I_0\right)\right). \end{aligned} \tag{3.4.1}$$

On the other hand, we can compute the topological charge explicitly in terms of

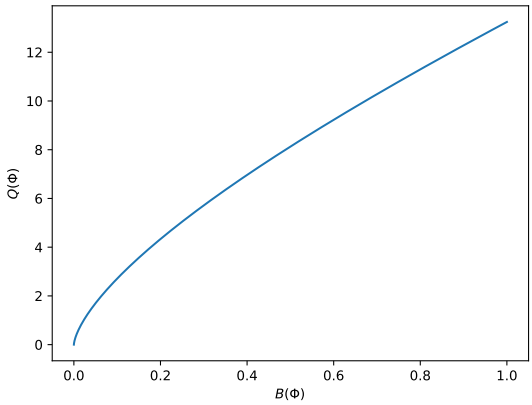

Figure 3.4.1: Parametric plot of the topological charge Q versus the baryonic charge B, both as a function of the magnetic flux Φ.

the magnetic flux using the expressions of Q (3.3.7), H (3.3.12) and Φ (3.3.16):

$$\begin{aligned} Q &= \frac{\pi^2 p^2 L_r}{K}[W(2\pi) - W(0)] \implies \\ Q &= \frac{4\sqrt{2}K\pi\Phi}{L_r}\sqrt{1 - \exp\left(-\frac{8K\Phi^2}{p^4(\pi L_r)^2} - 2I_0\right)}. \end{aligned} \tag{3.4.2}$$

It is interesting to compare the above expressions for both the baryonic and topological charge in order to see the nonlinearity of the system. From equations (3.4.1) and (3.4.2), it is possible to obtain the following relation:

$$\frac{Q}{B} = \frac{\pi^2\sqrt{K}}{\sqrt{1 - \exp\left(-\frac{8K\Phi^2}{p^4(\pi L_r)^2} - 2I_0\right)}} \tag{3.4.3}$$

In this way, we can plot the topological charge and the baryonic charge in order to illustrate the nonlinear relation between these two quantities (see Fig. 3.4.1).

As we can see, unlike non-interacting systems, there is a nonlinear dependency between the baryonic charge and the topological charge. However, as both the baryonic and topological charges increase, they enter a linear regime, just as expected.

3.5 On the boundary conditions of $H(r)$

The definition of the boundary conditions on $H(r)$ deserves a deeper discussion. From the physical point of view, the baryonic density ρ_B defined in Eqs. (2.1.12), (2.1.14) and (2.1.15) have to be interpreted physically and concretely as the *baryonic density*: namely, a density with the property that its integral is the baryonic charge. Thus, one could think that the only reasonable boundary conditions are the ones where the baryonic charge is an integer (and this is certainly a reasonable viewpoint). On the other hand, in situations in which the baryonic charge is very large (as in neutron stars) it is also possible to consider the baryonic charge as a continuous quantity. Indeed, variations of ± 1 baryons are very small compared to a total baryonic charge of the order of 10^{10}. Under these conditions, baryons can be considered as continuous variations of the mesonic field and the baryonic charge can be described as a continuous variable. In this subsection, we will show that in our case both viewpoints are reasonable and that the second one (where the baryonic charge is considered as a continuous variable) has some technical advantages (see also Section 4.3).

The boundary conditions on the functions appearing at the exponents of equation (2.1.4) are generally defined in such a way that the map U describes a closed manifold, isomorphic to an S^3 (see, for instance, [59] or [53]). Nevertheless, the introduction of the magnetic field defined by the ansatz (2.2.4) and the definition of the BPS equations (2.2.5) and (2.2.6) compromise the closure of the manifold. In particular, the map U introduced in (2.2.3) is isomorphic to S^3 with two points removed. A simple way to see this is the following. First of all, let us observe that, in order to get a closed manifold, one should impose the following boundary conditions on the exponent of (2.2.3)

$$0 \leq y \leq 2\pi, \qquad 0 \leq x \leq \pi. \tag{3.5.1}$$

Furthermore, H should be a continuous function on $0 \leq r \leq 2\pi$ such that (see, for instance, [52, 53, 62, 63, 64] for further details)

$$0 < H(r) < \frac{\pi}{2} \quad \text{or} \quad \frac{\pi}{2} < H(r) < \pi \quad \text{for} \quad 0 < r < 2\pi,$$

with boundary conditions

$$H(0) = \frac{\pi}{2} \quad \text{and} \quad H(2\pi) = 0 \tag{3.5.2}$$

for the first case, or

$$H(0) = \frac{\pi}{2} \quad \text{and} \quad H(2\pi) = \pi \tag{3.5.3}$$

for the second case (notice that $\sin(H(r))$ decreases, due to (3.3.12)). The condition (3.5.1) is automatically satisfied by the definition of the space in which the system is defined. On the other hand, the BPS equations (2.2.5) and (2.2.6) lead to the solution for $H(r)$ outlined in (3.3.12). It is straightforward to observe from here that $\sin H(r) \neq 0$ for each r, thus avoiding the *ending points* defined in (3.5.2) or (3.5.3). The condition $H(0) = \pi/2$ can be obtained when $I_0 = 0$, but in this case the relation (3.3.14) implies that $v(0) = v(2\pi) = 0$, thus leading to $H(r) = \pi/2$ for each r. One can deduce that $H(r)$ does not span the whole interval necessary to close the manifold. This, clearly, also affects the baryonic charge. Indeed, B only depends on the boundary conditions of $v(r)$ and $H(r)$, as arises from (2.1.12) and (2.2.8). For closed manifolds, B takes integer values. In our case, the boundary conditions of $v(r)$ and $H(r)$ are linked together using the equations (3.3.12) and (3.3.14). In particular, it is possible to define I_0 in terms of $v(2\pi)$ through equation (3.3.14) and $v(2\pi)$ in terms of $H(2\pi)$ through equation (3.3.12) (notice that, when we fix $v(0) = 0$, then I_0 only depends on the choice of $H(0)$). Therefore, one can write the value of B in terms of $H(2\pi)$, $v(2\pi)$ or I_0. For instance, we can define everything in terms of I_0, which now can assume arbitrary values, since it is not constrained by the *closeness conditions* of the manifold. This way, the baryonic charge B varies continuously with I_0.

It is worth mentioning here that the solutions to the equations (3.3.8) and (3.3.9) describe systems with $E = Q$, where $Q > 0$, unless $I_0 = 0$, in which case we have the trivial condition $Q = 0$. The parameter I_0 can be used to define a continuous deformation of the solutions with $Q > 0$ to solutions with $Q = 0$. In this sense, the system is not *topologically stable*. Nevertheless, once all the boundary conditions are fixed, the solutions have finite energy for $I_0 \neq 0$.

Interestingly, when $I_0 \to \infty$, then $H(r) \to 0$. In this case, the map U does not wrap around S^3 at all. The contribution to the baryonic charge is given entirely by the presence of the magnetic field (in particular, it derives from the volume

integral of (2.1.15), since the volume integral of (2.1.14) is zero). In this situation, the quantity Q defined in (3.3.7), only differs from B by a multiplicative constant. Explicitly,

$$B = 8p^2\pi\sqrt{K}L_r \qquad \text{and} \qquad Q = \pi^2\sqrt{K}B.$$

Therefore, the obtained solution is characterized by $E = Q > 0$, where the positivity of the energy is guaranteed only by the magnetic field contribution.

Now, two questions are in order. Are the solutions obtained from (3.3.8) and (3.3.9) stable for fixed values of B? What is the interpretation of the quantity B in this paradigm?

In order to answer these questions, we need to observe that both B and Q only depend on the boundary conditions. Once the latter are fixed, B and Q are invariant under the symmetries of the system. Then, for each sector characterized by B fixed, also Q is fixed and the energy associated with solutions to the Skyrme equations (2.2.5) and (2.2.6) has a finite minimum given by equation (3.3.7). This minimum is reached by the solutions to the BPS equations (3.3.8) and (3.3.9). Furthermore, we give B its original interpretation of *baryonic charge*. From a physical point of view, the fact that it can assume continuous values could be interpreted as due to a quantum correction that screens the baryonic charge. This interpretation would deserve a deeper investigation at a more fundamental level, but this is out of the scope of this thesis.

3.6 Approximation

For the development of this work, it is essential to find an analytic relation between the baryonic charge B, the topological charge Q, and the magnetic flux Φ. This requires determining an analytic expression for the integration constant I_0. To this end, we define the function F, which depends on both Φ and I_0, as follows:

$$F(\Phi, I_0) = \int_0^{\frac{\sqrt{2K}}{p^2\pi L_r}\Phi} \frac{d\tau}{\sqrt{1-\exp(-4\tau^2-2I_0)}}. \tag{3.6.1}$$

Unfortunately, it is not possible to obtain a closed form expression for this integral. However, an accurate analytic approximation can be obtained using standard Casimir effect techniques (see [66] and references therein), based on the expansion

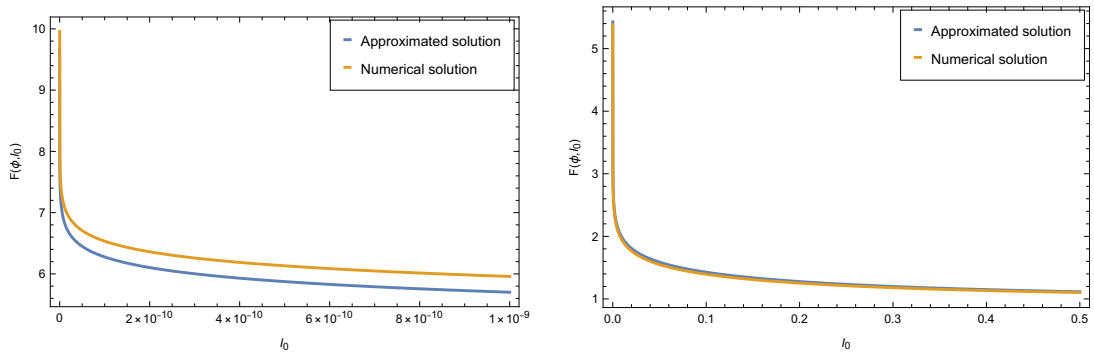

(a) **(b)**

Figure 3.6.1: Comparison between the analytic approximation and the numerical integration of (3.6.1), both for small values of I_0 (Fig. 3.6.1a) and for large values of I_0 (Fig. 3.6.1b). Here $\sqrt{2K}\Phi/(p^2\pi L_r) = 1$ (which corresponds to $\Phi \approx 10^5$ fm^2, see Section 4.1 for a discussion of the units of measure).

of the integral in terms of Bessel functions.

In this way, for $I_0 > 0$ we obtain the following analytic approximations for the integral (3.6.1). As shown in Fig. 3.6.1, these analytic expressions are in excellent agreement with the numerical results.

$$F(\Phi, I_0) \approx \frac{\sqrt{2K}}{p^2\pi L_r}\Phi - \frac{1}{4}\ln\left(1 - e^{-2I_0}\right) \tag{3.6.2}$$

$$F(\Phi, I_0) \approx \frac{1}{4}\log\left(1 + \frac{8K^2\Phi^2}{p^4\pi^2 L_r^2 I_0} + \sqrt{\frac{8K^2\Phi^2}{p^4\pi^2 L_r^2 I_0}\left(2 + \frac{8K^2\Phi^2}{p^4\pi^2 L_r^2 I_0}\right)}\right). \tag{3.6.3}$$

Note that (3.6.2) fails for $I_0 \to 0$. Indeed, the approximated expression (3.6.2) diverges for very small values of I_0. In this limit, we use the expression (3.6.3).

The explicit computation of these approximations is reported in Appendix A.

From (3.6.2) and (3.6.3), and given that $F(\Phi, I_0) = 2\pi L_r\sqrt{K}$, one can explicitly determine $v(2\pi)$ in terms of I_0. Namely,

$$v(2\pi)(I_0) \approx \begin{cases} \left[2\pi\sqrt{K}L_r + \frac{1}{4}\ln\left(1 - e^{-2I_0}\right)\right] & \text{For } I_0 \geq \varepsilon, \\ \sqrt{\frac{I_0}{2}}\sinh(4\pi\sqrt{K}L_r) & \text{For } I_0 < \varepsilon, \end{cases} \tag{3.6.4}$$

where ε is a positive, real quantity that minimizes the error of the approximation with respect to the original relation $F(\Phi, I_0) = 2\pi L_r\sqrt{K}$. This quantity can be determined numerically (in our case, it is of the order of $I_0 \approx 10^{-12}$). In Fig. 3.6.2, the comparison between the function (3.6.4) and $v(2\pi)$ obtained through a numerical solution of $F(\Phi, I_0) = 2\pi L_r\sqrt{K}$ is shown.

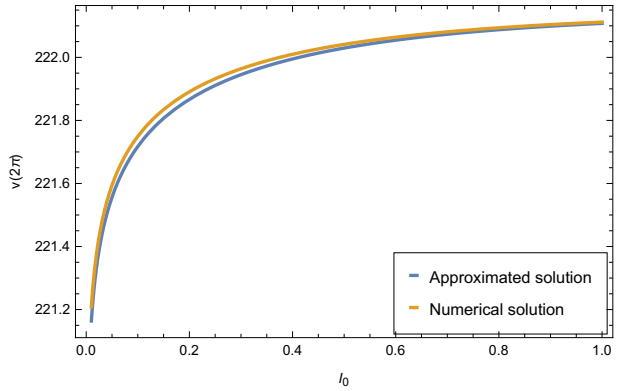

Figure 3.6.2: Comparison between the analytic approximation of $v(2\pi)$ (3.6.4) and the numerical solution of $F(\Phi, I_0) = 2\pi L_r\sqrt{K}$. Here F is defined in (3.6.1), where $K = 2$ fm^{-2} and $L_r = 25$ fm.

Through the equation (3.6.4), we can obtain analytically the dependence of I_0 in terms of the boundary condition $v(2\pi)$:

$$I_0(v(2\pi)) \approx \begin{cases} -\frac{1}{2}\log\left[1 - \exp\left(4v(2\pi) - 8\pi\sqrt{K}L_r\right)\right] & \text{For } v(2\pi) \geq \tilde{\varepsilon}, \\ v^2(2\pi)\frac{2}{\sinh^2(4\pi\sqrt{K}L_r)} & \text{For } v(2\pi) < \tilde{\varepsilon}, \end{cases} \tag{3.6.5}$$

where $\tilde{\varepsilon}$ plays the same role as ε in (3.6.4). This approximation can be used to define analytic expression for the quantities B and E in terms of $v(2\pi)$, which, in the general case, have the form

$$B = 4p^2 v(2\pi)\left(1 - e^{-4v^2(2\pi) - 2I_0}\right), \tag{3.6.6}$$

$$E = 4p^2\pi^2\sqrt{K}v(2\pi)\sqrt{1 - e^{-4v^2(2\pi) - 2I_0}}, \tag{3.6.7}$$

where I_0 can be replaced with (3.6.5).

Chapter 4

Thermodynamics

In this chapter, we transition from the classical field description of isolated baryonic layers to the macroscopic thermodynamic properties of a statistical ensemble of such configurations. Understanding the statistical mechanics of these systems is crucial for astrophysical applications, particularly for describing the behavior of dense nuclear matter and the so-called nuclear pasta phases inside neutron stars. First, in section 4.1, we establish the units of measure used throughout our thermodynamic analysis. Then, in sections 4.2 and 4.3, we compute the partition function considering both integer and continuous values for the topological charge B. Afterwards, in sections 4.4 and 4.5, we derive the fundamental thermodynamical quantities, culminating in the construction of the equation of state and the calculation of the speed of sound of the system. Finally, in section 4.6, we analyze the response of the system to an external field, evaluating the Maxwell equations and the magnetic susceptibility.

4.1 Units of measure

Before proceeding with the thermodynamic analysis, it is useful to establish the order of magnitude of the physical quantities under consideration. This will allow us to obtain numerical estimates of the thermodynamic quantities and to compare them with observational or experimental data.

At this point, a remark is necessary. The model developed in this work should be regarded as a preliminary framework. In particular, the solutions obtained here

are appropriate for describing baryonic crystals arranged in layered structures, reminiscent of the lasagna phase of nuclear matter expected in neutron stars. However, the actual physics of neutron stars is considerably more involved than the simplified description provided by our model. For example, nuclear pasta phases are typically embedded in a background medium consisting of nucleons in a liquid state together with an electron gas (see for instance [10]). In the present analysis we neglect the interaction with this surrounding medium, although such effects are essential for obtaining realistic estimates of the relevant physical quantities. The aim of this work is therefore to establish the foundations for a consistent treatment of these systems, which are otherwise extremely difficult to analyze using purely analytical methods. More complete treatments will be explored in future work.

With this in mind, we set $L_r \simeq 25$ fm. Due to the constraint (3.3.3), the lengths of the remaining edges of the box, denoted by L, depend on the parameter p. Consequently, this quantity cannot be fixed independently. The volume of the system is given by $V = 4\frac{2\pi^3 p^2 L_r}{2K}$.

Finally, we adopt the following conventional values for the constants

$$f_\pi = 2\sqrt{2}\ \text{fm}^{-1} \simeq 180\ \text{MeV}\ (K = \frac{f_\pi^2}{4} = 2\ \text{fm}^{-2}). \tag{4.1.1}$$

4.2 Integer values of B

From the expression for the baryonic charge (3.6.6), and replacing in it the approximation for $v(2\pi)$ given in (3.6.4), we can observe that the quantity B/p^2 possesses a maximum value. Indeed, by taking the limit $I_0 \to \infty$, we obtain

$$\lim_{I_0 \to \infty} \frac{B}{p^2} = 8\sqrt{K} L_r \pi. \tag{4.2.1}$$

whose value depends on the choice of the parameters of the system, as can be observed in Fig. 4.2.1.

As mentioned in the previous chapters, since the baryonic charge B represents the number of baryons in the system, it is natural to associate this quantity with an integer. To analyze this case, we will consider the values of $v(2\pi)$ for which

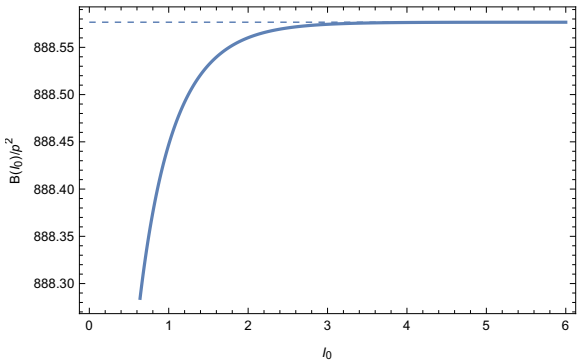

Figure 4.2.1: B/p^2 as a function of I_0. Here $K = 2$ fm^{-2}, $L_r = 25$ fm (The dashed line represents the maximal value obtained for $I_0 \to \infty$).

$B/p^2 = n$, where, in order for B to be an integer, n must also be an integer (in this case this condition has to be imposed by hand). As shown in (4.2.1), n has an upper bound, whose maximum value is $n_{max} = [8\sqrt{K}L_r\pi]$, where the square brackets denote the integer part. If the width of the layers increases, that is, if L_r increases, the maximum value of n also grows (since n scales linearly with L_r). In our case, we will use $L_r = 25$ fm which gives $n_{max} = 888$, for the analysis of the following sections. However, due to this large number of baryons, the analysis with a discrete baryonic charge becomes computationally demanding. For this reason, in this section we will use smaller values, namely $L_r = 1$ fm, which corresponds to $n_{max} = 35$. Later, we will analyze the case of large L_r, for which we will introduce a continuum extension of the baryonic charge.

The values of $v(2\pi)$ that satisfy $B/p^2 = n$ were determined numerically, as shown in Fig. 4.2.2. It can be observed that $v(2\pi)$ enters on a linear regime for large values of n.

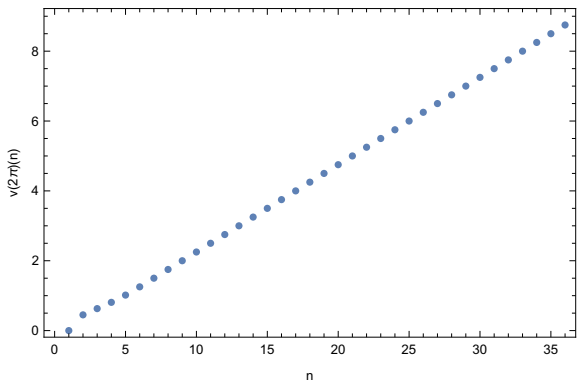

Figure 4.2.2: Values of $v(2\pi)(n)$ as a solution of the equation $B/p^2 = n$. Here $K = 2$ fm^{-2}, $L_r = 1$ fm.

As noted before, $v(2\pi)$ is practically linear over the entire range of n. This behavior will be useful later in our analysis.

4.2.1 The partition function

Based on the discussion above, we can define the grand canonical partition function of the system as:

$$\mathcal{Z}(\beta, \mu_B) = \sum_{p=-\infty}^{+\infty} \sum_{n=1}^{n_{max}} e^{-\beta(E-\mu_B B)}, \tag{4.2.2}$$

where $\beta = 1/T$ is the inverse temperature, E is the energy defined in (3.6.7), μ_B is the baryonic chemical potential, and B is the baryonic charge defined in (3.6.6).

Notice that both E and B share the common factor p^2. Therefore, we can factor out p^2 from the exponent of the partition function, obtaining

$$\mathcal{Z}(\beta, \mu_B) = \sum_{p=-\infty}^{+\infty} \sum_{n=1}^{n_{max}} e^{-\beta p^2 \mathcal{F}(n,\mu_B)}, \tag{4.2.3}$$

where we define $\mathcal{F}$ as the free energy in units of p^2. By explicitly substituting the expressions for E and B into the exponent, we obtain the following expression for the free energy

$$\mathcal{F}(n, \mu_B) = 2\pi^2 \sqrt{nK} \sqrt{v(2\pi)(n)} - n\mu_B, \tag{4.2.4}$$

whose behavior is shown in Fig. 5.3.5a.

Note that the quantity $v(2\pi)$ is expressed as a function of n. On the other hand, the sum over p converges only if $\mathcal{F}(n, \mu_B) > 0$. This condition is satisfied when

$$\mu_B < \mu_B^*(n), \quad \text{with} \quad \mu_B^*(n) = \frac{\mathcal{F}(n, \mu_B = 0)}{n}. \tag{4.2.5}$$

The values of μ_B^* are shown in Fig. 4.2.3b. Since μ_B^* converges to a constant value as n increases, in order for the inequality $\mathcal{F}(n, \mu_B) > 0$ to be satisfied for every n, we must consider the value of $v(2\pi)(n)$ evaluated in n_{max}, which we denote as $\tilde{\mu}_B = \mu_B^*(n_{max})$. Once these convergence criteria are satisfied, the sum over p

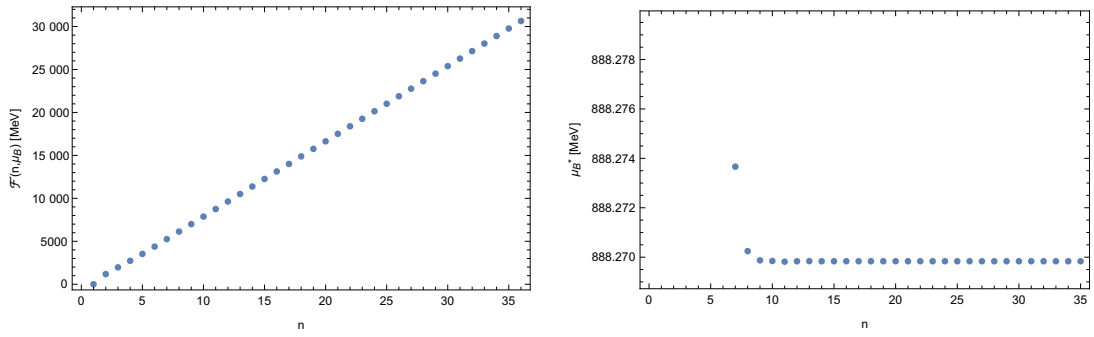

(a) **(b)**

Figure 4.2.3: Free energy $\mathcal{F}$ as a function of n for $\mu_B = 0.2$ (Fig. 5.3.5a), and critical chemical potential μ_B^* as a function of n (Fig. 4.2.3b). For large n, $\mathcal{F}$ becomes linear while μ_B^* approaches a constant value. Here $K = 2$ fm^{-2} and $L_r = 1$ fm.

leads to the well-known theta function θ_3 (see Appendix B and [67]). To simplify the notation from this point onward, we introduce the function

$$\xi(\tau) = \theta_3(e^{i\pi\tau}). \tag{4.2.6}$$

Therefore,

$$\sum_{p=-\infty}^{\infty} e^{-\beta p^2 \mathcal{F}(n,\mu_B)} = \xi\left(\frac{i\beta}{\pi}\mathcal{F}(n,\mu_B)\right). \tag{4.2.7}$$

Note that the theta function (4.2.7) diverges when $n = 0$, since $\mathcal{F}(0,\mu_B) = 0$. For this reason, we define the sum in the partition function to run from 1 to n_{max}. Moreover, this is equivalent to considering only states with non–vanishing baryonic charge, which is necessary for the formation of the layers. In this way, the partition function reduces to

$$\mathcal{Z}(\beta,\mu_B) = \sum_{n=1}^{n_{max}} \xi\left(\frac{i\beta}{\pi}\mathcal{F}(n,\mu_B)\right). \tag{4.2.8}$$

This sum clearly converges to a finite value, since n is bounded from both below and above. The behavior of the partition function $\mathcal{Z}$ as a function of β and μ_B is illustrated in Fig. 4.2.4.

Let us briefly pause to make the following observations. Recall that when $I_0 \to \infty$,

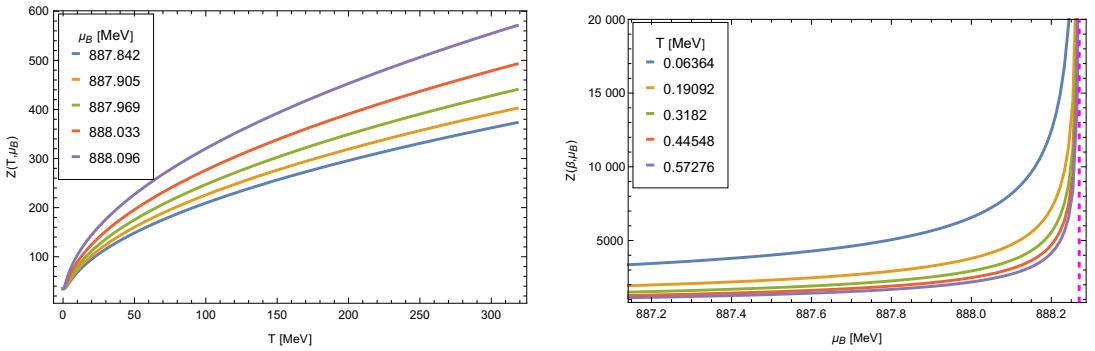

(a) **(b)**

Figure 4.2.4: Partition function $\mathcal{Z}(T, \mu_B)$ as a function of $T = 1/\beta$ and μ_B . Here $K = 2$ fm^{-2} and $L_r = 1$ fm. The dashed line in (Fig. 4.2.4b) represents the value of $\tilde{\mu}_B$.

n reaches its maximum value n_{max}. Consequently,

$$1 - \exp\left(4v(2\pi) - 8\pi\sqrt{K}L_r\right) \to 0. \tag{4.2.9}$$

In this limit, it follows from the expression for the baryonic charge (3.6.6) that $v(2\pi) \propto n$. More specifically, in this limit we obtain

$$v(2\pi) = \frac{n}{4}. \tag{4.2.10}$$

In this regime, the energy (3.6.7) is also proportional to n. This behavior can be visualized in Fig. 4.2.2, which suggests that the free energy $\mathcal{F}$ is also proportional to n for sufficiently large values of n, as shown in Fig. 4.2.3. In particular, in this regime $\mathcal{F}$ can be approximated as

$$\mathcal{F}(n, \mu_B) \approx n\left[\tilde{\mu}_B - \mu_B\right], \tag{4.2.11}$$

with $\tilde{\mu}_B = \pi^2 K$. When $\mu_B \approx \tilde{\mu}_B$, then $\mathcal{F}(n, \mu_B) \approx 0$ and the theta function diverges. The degree of the divergence can be studied through the identity (see Appendix B)

$$\xi(\tau) = \frac{1}{\sqrt{-i\tau}}\xi\left(-\frac{1}{\tau}\right). \tag{4.2.12}$$

In our case, $\tau = \frac{i\beta}{\pi}\mathcal{F}(n,\mu_B)$. Therefore, the function $\xi(\tau)$ can be written as

$$\xi\left(\frac{i\beta}{\pi}\mathcal{F}(n,\mu_B)\right) = \frac{1}{\sqrt{\frac{\beta}{\pi}\mathcal{F}(n,\mu_B)}}\left(1+2\sum_{p=1}^{\infty}q^{p^2}\right). \tag{4.2.13}$$

where $q = \exp\left(-\frac{\pi 2}{\beta\mathcal{F}(n,\mu_B)}\right)$. When $\beta(\tilde{\mu}_B - \mu_B)$ is small enough, then $q \approx 0$ and

$$\xi\left(\frac{i\beta}{\pi}\mathcal{F}(n,\mu_B)\right) \approx \frac{1}{\sqrt{\frac{\beta}{\pi}n\left[\tilde{\mu}_B - \mu_B\right]}}. \tag{4.2.14}$$

Notably, this approximation is valid also when n is small. In this case, $\tilde{\mu}_B$ is replaced by $\mu_B^*(n)$ and β is small enough.

This divergence shows that $\tilde{\mu}_B$ represents the maximum value of the chemical potential, beyond which the present analysis is no longer reliable (see also the discussion in Section 4.4). It is important to stress that deriving a finite range for the baryonic chemical potential through an explicit analytic expression constitutes a remarkable result, especially in light of the well-known difficulties encountered by Lattice QCD at finite baryon density.

4.3 Continuous values of B

As mentioned previously, when considering a large number of baryons, the difference between B and $B+1$ becomes negligible. Therefore, we can ignore the assumption that B takes only integer values and instead adopt a continuum approximation. In fact, our model allows n to vary continuously between 0 and n_{max}. This can be interpreted as an effective quantum screening of the baryonic charge, allowing it to be treated as a continuous variable.

Moreover, the analysis of a continuous baryonic charge becomes particularly relevant when the width of the layers is large. In this case, as discussed in the previous chapter, we consider $L_r = 25$ fm, which corresponds to $n_{max} \approx 888.58$. The behavior of the partition function analyzed in the discrete case can be extended to the continuous case by considering the following.

When n is treated as a continuous variable, the sum in the partition function becomes an integral, giving

$$\mathcal{Z}(\beta, \mu_B) = \int_0^{n_{max}} \xi\left(\frac{i\beta}{\pi}\mathcal{F}(n, \mu_B)\right)\, dn, \tag{4.3.1}$$

where now $n_{max} = 8\sqrt{K}L_r\pi$ is a real number. The behavior of the partition function for continuous n, as a function of the temperature T and the baryonic chemical potential μ_B, is shown in Fig. 4.3.1.

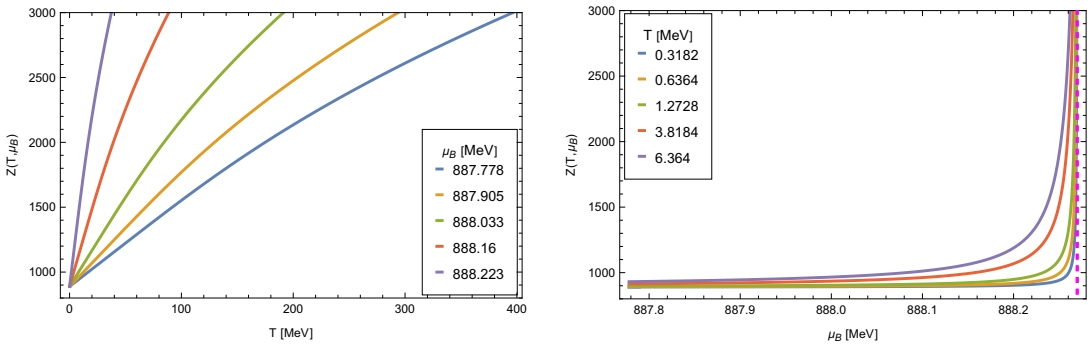

(a) **(b)**

Figure 4.3.1: Partition function $\mathcal{Z}(T, \mu_B)$ as a function of $T = 1/\beta$ and μ_B . Here $K = 2$ fm^{-2} and $L_r = 25$ fm. The dashed line in (Fig. 4.3.1b) represents the value of $\tilde{\mu}_B$.

Note that, as $n \to 0$, the theta function diverges as $n^{-\frac{1}{2}}$. Therefore, the integral remains convergent.

Interestingly, taking this continuum approximation leads to a connection with the Riemann zeta function when n_{max} is large. Indeed, if we consider the following function

$$\Theta(x) = \xi(ix), \tag{4.3.2}$$

it holds

$$\int_0^\infty x^{\frac{s}{2}-1}(\Theta(x) - 1)dx = 2\frac{\Gamma(s/2)}{\pi^{s/2}}\zeta(s), \tag{4.3.3}$$

for any s such that $Re(s) > 0$. In this situation, assuming $\beta(\tilde{\mu}_B - \mu_B)$ not too small, we can approximate $\mathcal{F}(n, \mu_B) \approx n\,[\tilde{\mu}_B - \mu_B]$. Furthermore, let us define

$$\tilde{\mathcal{Z}}(\beta, \mu_B) = \mathcal{Z}(\beta, \mu_B) - n_{max}. \tag{4.3.4}$$

Thus,

$$\begin{aligned}\tilde{\mathcal{Z}}(\beta, \mu_B) &\simeq \int_0^\infty \left[\Theta\left(\frac{\beta}{\pi}\mathcal{F}(n, \mu_B)\right) - 1\right] dn \\ &= \frac{2}{\beta}\frac{\zeta(2)}{\tilde{\mu}_B - \mu_B} = \frac{\pi^2}{3\beta(\tilde{\mu}_B - \mu_B)}.\end{aligned} \tag{4.3.5}$$

More generally, one can compute the expectation value of an extensive quantity $Q(n) = wn^s$ as

$$\begin{aligned}\langle Q(n)\rangle &\simeq \frac{w}{\mathcal{Z}(\beta, \mu_B)}\int_0^\infty \left[\Theta_3\left(\frac{\beta}{\pi}\mathcal{F}(n, \mu_B)\right) - 1\right] n^s\, dn \\ &= \frac{w}{\beta^s}\frac{1}{(\tilde{\mu}_B - \mu_B)^s}\Gamma(s+1)\frac{\zeta(2s+2)}{\zeta(2)}.\end{aligned} \tag{4.3.6}$$

This expression receives two types of corrections. The first arises from the finiteness of $n_{\max}$ and leads to terms of order $e^{-\beta n_{\max}(\tilde{\mu}_B - \mu_B)}$. Consequently, the formula cannot be reliably applied when $\beta n_{\max}(\tilde{\mu}_B - \mu_B)$ is small. The second source of corrections originates from the fact that the behavior of μ_B^* changes for small values of n. In particular, by using Eqs. (4.2.4) and (4.2.5), we can explicitly write

$$\mathcal{F}(n, \mu_B) = n\,[\mu_B^*(n) - \mu_B]\,, \tag{4.3.7}$$

$$\mu_B^*(n) = 2\pi^2 K^{\frac{1}{2}}\sqrt{\frac{v(2\pi)(n)}{n}}. \tag{4.3.8}$$

In order to express $v(2\pi)$ in terms of n, we need to solve the relation $B/p^2 = n$.

To this end, we consider Eq. (3.6.6) using the approximations (3.6.5). The explicit expression for B/p^2 then reads

$$\frac{B}{p^2} \approx \begin{cases} 4v(2\pi)\left[1 - e^{-4v^2(2\pi)}(1 - e^{4v(2\pi)-8\pi\sqrt{K}L_r})\right] & \text{for } v(2\pi) \geq \tilde{\varepsilon}, \\ 4v(2\pi)\left[1 - e^{-4v^2(2\pi)\left(1+\frac{1}{\sinh^2(4\pi\sqrt{K}L_r)}\right)}\right] & \text{for } v(2\pi) < \tilde{\varepsilon}. \end{cases} \tag{4.3.9}$$

Since the second relation holds for very small values of $v(2\pi)$, in this limit we can write

$$\frac{B}{p^2} \approx 16v^3(2\pi)\left(1 + \frac{1}{\sinh^2(4\pi\sqrt{K}L_r)}\right). \tag{4.3.10}$$

Then,

$$v(2\pi) \approx \left[\frac{n}{16\left(1 + \sinh^{-2}(4\pi\sqrt{K}L_r)\right)}\right]^{\frac{1}{3}} \tag{4.3.11}$$

for very small $v(2\pi)$. The exact value of $v(2\pi)$ for values that are not very small must be determined numerically. However, Fig. (4.3.2) indicates that the dependence of n on $v(2\pi)$ (and vice versa) is approximately linear when $n_{\max}$ is large. In particular, from Fig. 4.3.2b it is evident that the linear approximation remains valid starting from relatively small values of $v(2\pi)$ (around 0.8, corresponding to $n \approx 3.2$).

In the following, we employ the linear approximation for $v(2\pi)$ in order to simplify the computations.

4.4 Thermodynamical quantities

The BPS tools that we have discussed offer us the unique opportunity to study the thermodynamics of interacting systems. When studying thermodynamics, one usually considers free gases (without interaction), but here, as can be seen in the relation between the topological charge and the baryonic charge (3.4.3), this system is clearly interacting.

Since we have obtained an explicit expression for the grand canonical partition

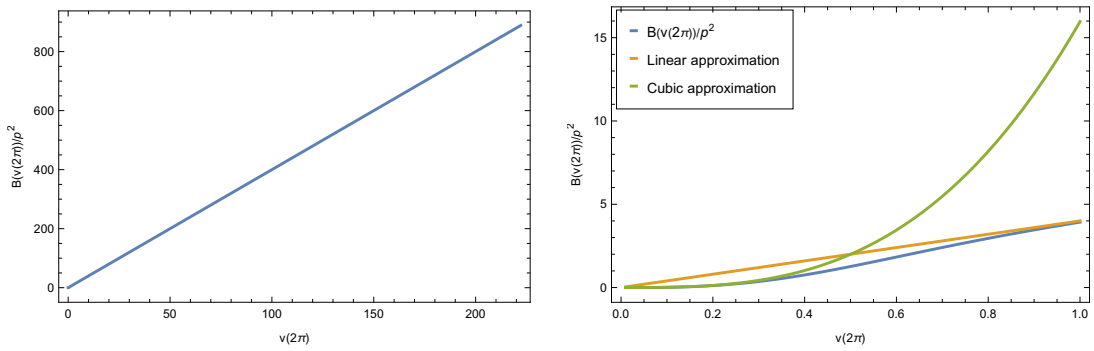

(a) **(b)**

Figure 4.3.2: Values of $B/p^2 = n$ in terms of $v(2\pi)$. Here $K = 2$ fm^{-2} and $L_r = 25$ fm. The (Fig. 4.3.2a) illustrates the relationship across the full range of $v(2\pi)$. In contrast, (Fig. 4.3.2b) displays the same relationship for small values of $v(2\pi)$, comparing it against the approximation (4.3.11) and the linear approximation $n = v(2\pi)/4$.

function of the system, we can now compute several thermodynamic quantities as functions of the temperature T and the baryonic chemical potential μ_B. The thermodynamic quantities analyzed in this section are the following:

Internal energy:

$$U = -\frac{\partial \ln \mathcal{Z}}{\partial \beta}; \tag{4.4.1}$$

Entropy:

$$S = k_B \left[\ln \mathcal{Z} - \beta \frac{\partial \ln \mathcal{Z}}{\partial \beta} \right]; \tag{4.4.2}$$

Average number of particles:

$$\langle N \rangle = \frac{1}{\beta} \frac{\partial \ln \mathcal{Z}}{\partial \mu_B}; \tag{4.4.3}$$

Heat capacity:

$$C_V = k_B \beta^2 \frac{\partial^2 \ln \mathcal{Z}}{\partial \beta^2}. \tag{4.4.4}$$

where, recall that $\beta = 1/k_B T$, with T being the temperature and k_B the Boltzmann constant (which we set equal to 1 from this point onward). The behavior of these thermodynamic quantities is shown in Figs. 4.4.1, 4.4.2, 4.4.3, and 4.4.4. In some cases, we have considered relatively high temperatures in order to better visualize their behavior.

The plots in Fig. 4.4.1 are particularly relevant, as they reveal the existence of

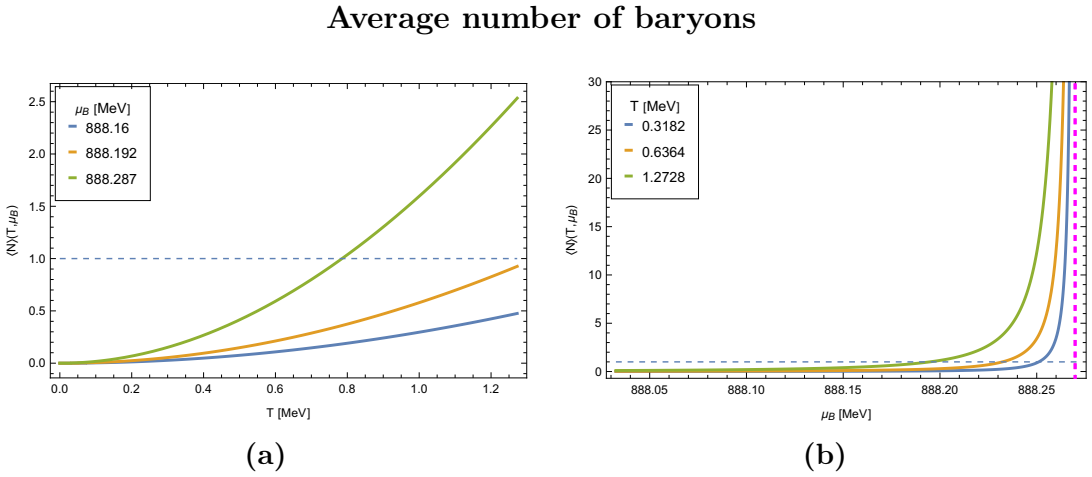

Figure 4.4.1: Average numbers of baryons as a function of the temperature T (Fig. 4.4.1a) and baryonic chemical potential μ_B (Fig. 4.4.1b). Here $K = 2\ \mathrm{fm}^{-2}$ and $L_r = 25$ fm. The dashed horizontal line represents the case with $\langle N \rangle = 1$.

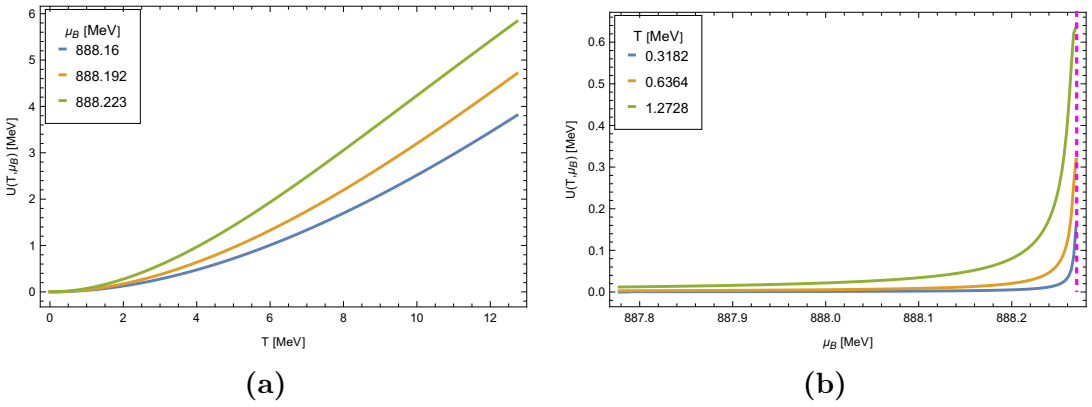

Figure 4.4.2: Internal energy as a function of temperature T (Fig. 4.4.2a) and baryon chemical potential μ_B (Fig. 4.4.2b). Here $K = 2\,\mathrm{fm}^{-2}$ and $L_r = 25\,\mathrm{fm}$.

lower bounds either for the temperature T at fixed values of μ_B (see Fig. 4.4.1a) or for the baryonic chemical potential μ_B at fixed values of T (see Fig. 4.4.1b). From Fig. 4.4.1a it follows that, once the baryonic chemical potential is fixed, the temperature must exceed a threshold value ($T \geq T_0(\mu_B)$) in order for at least one particle to be produced. Conversely, when the temperature is fixed, the baryonic chemical potential must satisfy $\mu_B \geq \mu_{B,0}(T)$.

Remarkably, when $\tilde{\mu}_B - \mu_B$ is sufficiently small, the allowed temperature range overlaps with the one typically associated with the formation of nuclear pasta,

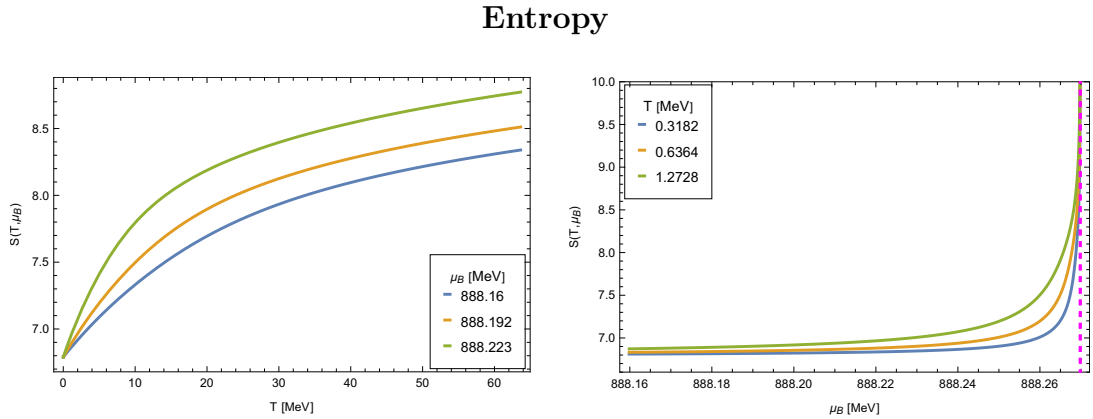

(a) **(b)**

Figure 4.4.3: Entropy as a function of temperature T (Fig. 4.4.3a) and baryon chemical potential μ_B (Fig. 4.4.3b). Here $K = 2\,\mathrm{fm}^{-2}$ and $L_r = 25\,\mathrm{fm}$.

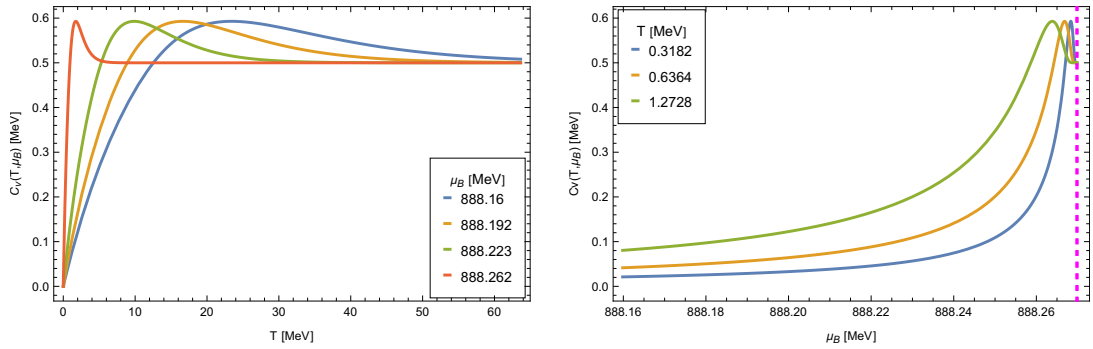

(a) **(b)**

Figure 4.4.4: Heat capacity as a function of temperature T (Fig. 4.4.4a) and baryonic chemical potential μ_B (Fig. 4.4.4b). Here $K = 2\ \mathrm{fm}^{-2}$ and $L_r = 25\ \mathrm{fm}$.

namely 0.5 MeV $\leq T \leq$ 15 MeV [10, 68]. This feature can be directly inferred from the approximation (4.2.14). In fact, when $\tilde{\mu}_B - \mu_B$ is very small, one obtains

$$\langle N \rangle \approx \frac{1}{2\beta(\tilde{\mu}_B - \mu_B)}. \tag{4.4.5}$$

Therefore, $\langle N \rangle > 1$ whenever $T > 2(\tilde{\mu}_B - \mu_B)$, taking $k_B = 1$. The lower bound for T approaches zero as μ_B approaches $\tilde{\mu}_B$. Nevertheless, one must keep in mind that T cannot coincide with this lower bound, otherwise the approximation

(4.2.14) ceases to be valid. Moreover, the case $\mu_B = \tilde{\mu}_B$ leads to divergences in some thermodynamic quantities. Consequently, the behavior of the system cannot be analyzed exactly at $T = 0$ MeV. However, by appropriately tuning μ_B, one can reach very low temperatures within the range typically associated with the formation of nuclear pasta.

It is also worth noting that the value $\tilde{\mu}_B \approx 888.27$ MeV obtained in our model is slightly smaller than the baryonic chemical potential usually associated with nuclear pasta formation, although it is not dramatically different. Indeed, typical estimates lie in the interval 930–1000 MeV (see, for instance, [69]).

As already observed in the case of integer baryonic charge, the limit $\tilde{\mu}_B$ cannot be exceeded. The divergent behavior exhibited by some thermodynamic quantities near this value may be interpreted as a signal of a phase transition. However, it should be emphasized that our model only describes a specific configuration of nuclear matter, namely layered baryonic structures. As a result, the possible existence of other phases cannot be explored within this framework. For this reason, $\tilde{\mu}_B$ should be regarded as a limit of validity for the present model.

Another noteworthy feature is that the model does not predict an upper bound for the temperature, which is usually associated with phase transitions. This suggests that the structures studied in this thesis may persist even at very high temperatures.

Examining the plots in Fig. (4.4.3), one observes that the entropy does not vanish in the limit $T \to 0$. This behavior originates from the presence of a degenerate state corresponding to $p = 0$. Indeed, when T becomes very small (so that $\beta \to \infty$), the only surviving contribution to the partition function comes from the ground state at $p = 0$. This state is characterized by vanishing volume, as a consequence of the relation (3.3.3) imposed to obtain the BPS conditions, and also by zero energy. Nevertheless, it can contain $0 \leq n \leq n_{max}$ layers, which leads to a degeneracy. In particular,

$$\lim_{\beta\to\infty} \mathcal{Z} = \int_{n=0}^{n_{max}} 1 \, dn = n_{max}. \tag{4.4.6}$$

As a result, the entropy becomes

$$\lim_{\beta\to\infty} S = k_B \ln(n_{max}). \tag{4.4.7}$$

Finally, the heat capacity C_v, shown in Fig. 4.4.4, displays a characteristic Schottky-like anomaly [70]. The position of the peak can be determined analytically by using the approximations (4.2.14) in the limit $\beta(\tilde{\mu}_B - \mu_B) \to 0$ and (4.3.5) for finite values of $\beta(\tilde{\mu}_B - \mu_B)$. Interestingly, for certain values of μ_B, the peak temperature occurs around $T \approx 10$–15 MeV, which corresponds to the temperature range usually associated with the transition from pasta-like structures to uniform nuclear matter [71]. As $\mu_B \to \tilde{\mu}_B$, this peak shifts toward $T \to 0$. Although the absence of a singular behavior (typically manifested as a λ-peak) suggests that no true thermodynamic phase transition is present, this feature deserves further investigation in future studies.

4.5 Equation of state and speed of sound

Using the BPS properties of the magnetic layers presented in Chapter 3, we can analytically derive the equation of state $P = P(\epsilon)$ (where P is the pressure and ϵ is the energy density), and from this compute the speed of sound c_s, defined by $c_s^2 = \partial P/\partial\epsilon$, which is subject to the causality condition $0 < c_s^2 \leq 1$.

To this end, we consider the energy-momentum tensor $T^{\mu}{}_{\nu} = g^{\mu\rho}T_{\rho\nu}$, which in matrix form takes the following structure:

$$T^{\mu}{}_{\nu} = \begin{pmatrix} -\epsilon & 0 & 0 & 0 \\ 0 & T_1 & 0 & 0 \\ 0 & 0 & T_2 & D \\ 0 & 0 & D & T_3 \end{pmatrix}, \tag{4.5.1}$$

where the energy density $\epsilon = T_{00}$ is defined in Eq. (2.2.7), while the remaining

components of the tensor are given by

$$T_1 = -\frac{K\left(p^2\cos^2 H + 4u^2\sin^2 H\right)}{L^2} + \frac{K(H')^2}{2L_r^2} + \frac{(u')^2}{L_r^2 L^2}, \tag{4.5.2}$$

$$T_2 = T_3 = -\frac{K(H')^2}{2L_r^2}, \tag{4.5.3}$$

$$D = \frac{K}{L^2}\left(p^2\cos^2 H - 4u^2\sin^2 H\right) - \frac{(u')^2}{L_r^2 L^2}. \tag{4.5.4}$$

To directly identify the energy density and the pressures of the system, we diagonalize the energy-momentum tensor, which then takes the following structure:

$$(T^{\mathrm{D}})^{\mu}{}_{\nu} = \begin{pmatrix} -\epsilon & 0 & 0 & 0 \\ 0 & T_1 & 0 & 0 \\ 0 & 0 & T_2 + D & 0 \\ 0 & 0 & 0 & T_2 - D \end{pmatrix}. \tag{4.5.5}$$

Using the BPS property $H = H(v)$ (3.3.12), we can express the energy density as $\epsilon = \epsilon(v)$, and similarly the pressures of the diagonalized energy-momentum tensor, obtaining:

$$\epsilon = 4K^2\left(1 + e^{-4v^2-2I_0}(4v^2-1)\right), \tag{4.5.6}$$

$$T_2 + D = -16K^2v^2e^{-4v^2-2I_0}, \tag{4.5.7}$$

$$T_2 - D = T_1 = 0. \tag{4.5.8}$$

The trace of the energy-momentum tensor takes the form $(T^{\mathrm{D}})^{\mu}{}_{\mu} = -\epsilon + 3P$, assuming that the system behaves as a perfect fluid without dissipation. In this way, we can write the total pressure of the system as follows

$$P = \frac{1}{3}(T_2 + D) = -\frac{16}{3}K^2v^2e^{-4v^2-2I_0}. \tag{4.5.9}$$

Remarkably, Eq. (4.5.6) can be inverted, allowing us to obtain $v = v(\epsilon)$ in closed analytic form:

$$v(\epsilon) = \pm\frac{1}{2}\sqrt{1 - W_0\left(\left(1 - \frac{\epsilon}{4K^2}\right)e^{1+2I_0}\right)}, \tag{4.5.10}$$

where W_0 denotes the principal branch of the Lambert W function. By substituting this expression for $v(\epsilon)$ into (4.5.9), we obtain an analytic expression for the equation of state $P(\epsilon)$:

$$P(\epsilon) = \frac{4}{3}K^2\left(1 - \frac{\epsilon}{4K^2} - e^{-1-2I_0+W_0\left[\left(1-\frac{\epsilon}{4K^2}\right)e^{1+2I_0}\right]}\right). \tag{4.5.11}$$

Note that the energy density ϵ must satisfy the following inequality in order to ensure that $v(\epsilon)$ takes real values: $W_0\left[\left(1 - \frac{\epsilon}{4K^2}\right)e^{1+2I_0}\right] \leq 1$, due to the square root appearing in Eq. (5.5.10). As a consequence, the system exhibits negative pressure, as can be seen in Fig. 4.5.1, as given by the equation of state (4.5.9).

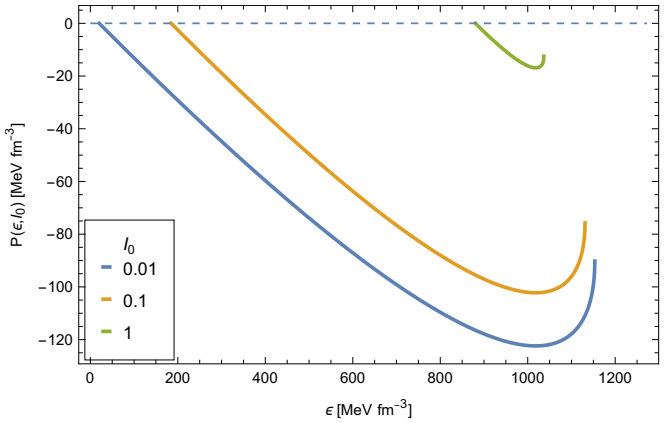

Figure 4.5.1: Equation of state as a function of ϵ for different values of I_0. Here $K = 2$ fm^{-2}, $L_r = 25$ fm.

The endpoints of the curves on Fig. 4.5.1 arise from the mathematical structure of the description, in particular from the appearance of the W Lambert function. Regions where the compressibility becomes negative are mechanically unstable and should therefore be replaced by a phase–coexistence construction; consequently, that branch of the equation of state is not physically realized [72].

It is also worth noting that negative values of the pressure indicate that the system tends to collapse. Such a result is not unexpected, since our analysis only considers states composed of purely baryonic dense matter. A more complete treatment should include the contribution of the electron gas, which plays a crucial role in

stabilizing the system and yielding a positive total pressure. Similar behaviors have been reported in [73, 74].

On the other hand, although at first glance one could say that in this work we study the thermodynamics of a classical system, since we have solved the classical equations of motion, the model is a semiclassical description of pions, and therefore there exist quantum effects that may justify why the pressure is negative.

The speed of sound c_s can be obtained by differentiating the equation of state (4.5.11) with respect to the energy density ϵ:

$$c_s^2 = \frac{\partial P}{\partial \epsilon} = \frac{1}{3}\left(\frac{1}{1 + W_0\left[\left(1 - \frac{\epsilon}{4K^2}\right) e^{1+2I_0}\right]} - 1\right). \tag{4.5.12}$$

Similarly, to ensure real and positive values of the speed of sound c_s^2, we must impose a constraint on the energy density. In this case, $c_s^2 \geq 0$ when

$$W_0\left[\left(1 - \frac{\epsilon}{4K^2}\right) e^{1+2I_0}\right] \leq 0. \tag{4.5.13}$$

Therefore, $\epsilon \geq 4K^2$. The behavior of the speed of sound c_s^2 is shown in Fig. 4.5.2.

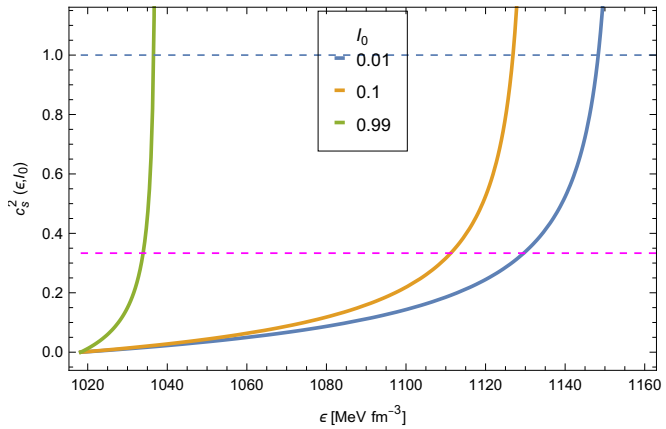

Figure 4.5.2: Speed of sound as a function of ϵ for different values of I_0. Here $K = 2$ fm^{-2}, $L_r = 25$ fm. The magenta line represents the conformal limit $c_s^2 = \frac{1}{3}$. The values of ϵ for which $c_s^2 > 1$ are not physical and are associated to the use of the Lambert function.

Here, let us highlight a couple of important points.

First, we observe that the speed of sound exceeds the conformal limit $\frac{1}{3}$ (as shown in Fig. 4.5.2). This behavior has also been found in other models describing dense

nuclear matter (see for instance [75]). On the other hand, in the case studied in this thesis, the speed of sound overcomes the speed of light, namely when $c_s^2 = 1$ (see Fig. 4.5.2), and diverges near the endpoints of the equation of state (see Fig. 4.5.1). Once again, this feature is likely an artifact of the model. In a more realistic scenario, the curves shown in Fig. 4.5.1 would extend beyond the endpoints, with the pressure eventually becoming positive and the system undergoing a phase transition at sufficiently high energy densities. In such a regime, the speed of sound would remain finite. However, the present model does not provide a reliable description of the system at these large energy densities.

A second aspect concerns the magnitude of the energy density itself. The constraints imposed by the model lead to values that are significantly larger than those typically associated with nuclear pasta, or more generally with dense nuclear matter.

Despite these limitations, the model still makes it possible to define an equation of state and to estimate the speed of sound. Achieving this, particularly through analytic methods, is generally a difficult task in the study of dense nuclear matter.

4.6 External field and magnetic susceptibility

In this section, we analyze the effects of an external magnetic field on the magnetized BPS baryonic layers. To this end, we introduce a perturbation of the magnetic field of the form

$$v(r) \to v(r) + b_e r, \tag{4.6.1}$$

where b_e denotes the magnitude of the external magnetic field, which is taken to be arbitrarily small. This perturbation also induces a small variation in $H(r)$, so that

$$H(r) \to H(r) + I(r, b_e), \tag{4.6.2}$$

where $I(r, b_e)$ is a function of both r and the external field b_e, which must be determined. Its natural to impose the following condition on this function,

$$I(r,0)=0. \tag{4.6.3}$$

Since b_e is small, we expand $I(r,b_e)$ to first order in b_e, obtaining

$$I(r,b_e)\simeq b_e\frac{\partial I(r,0)}{\partial b_e}=b_e\eta(r), \tag{4.6.4}$$

Here, we used the condition (4.6.3). In this way, the equation of motion for H (2.2.5), at first order in b_e, becomes

$$\begin{aligned} &H''+4\left(\frac{L_r}{\bar{L}}\right)^2\sin(2H)\left(\frac{1}{4}-v^2\right)\\ &\quad+b_e\left\{\eta''+8\left(\frac{L_r}{\bar{L}}\right)^2\left[\eta\cos(2H)\left(\frac{1}{4}-v^2\right)-vr\sin(2H)\right]\right\}=0, \end{aligned} \tag{4.6.5}$$

where the prime denotes the derivative with respect to r, and $\bar{L}=\frac{L}{p}$. The functions H and u correspond to the solutions of the BPS equations (3.3.8) and (3.3.9). Consequently, the terms in Eq. (4.6.5) that are independent of b_e are automatically satisfied. The remaining part of the equation then provides a differential equation for the perturbation η. Using the relations (3.3.12), we can express H in terms of v. In particular,

$$\cos(2H)=1-2e^{-4v^2-2I_0} \tag{4.6.6}$$

$$\sin(2H)=2e^{-2v^2+2I_0}\sqrt{1-e^{-4v^2-2I_0}} \tag{4.6.7}$$

In this way, the equation for η can be written as

$$\eta''+f\eta=g, \tag{4.6.8}$$

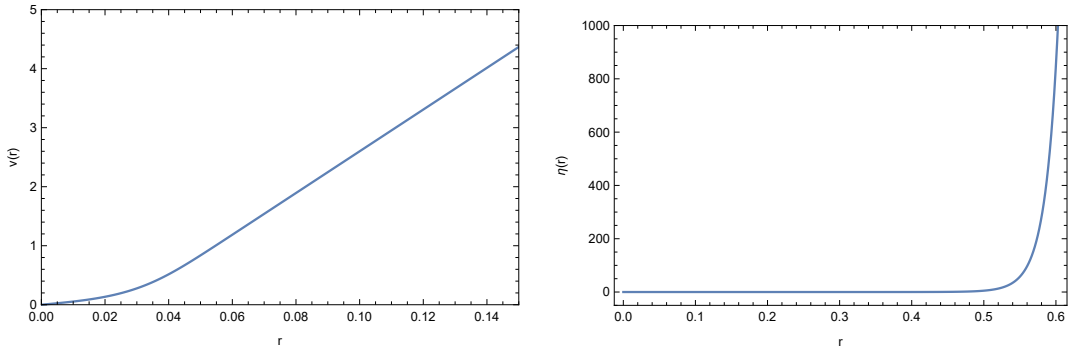

Figure 4.6.1: Numerical solution for $v(r)$ and $\eta(r)$. Here $K = 2$ fm^{-2}, $L_r = L = 25$ fm and $I_0 = 0.01$

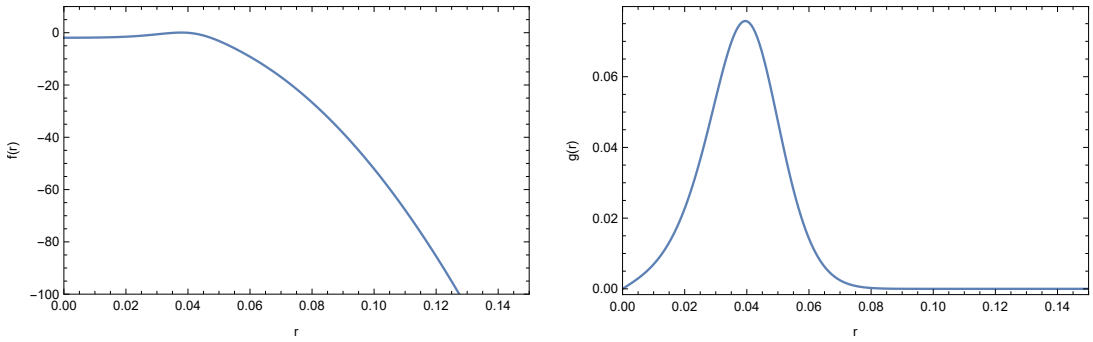

Figure 4.6.2: Numerical solution for $f(r)$ and $g(r)$. Here $K = 2$ fm^{-2}, $L_r = L = 25$ fm and $I_0 = 0.01$

where

$$f(v,r) = 2\left(\frac{L_r}{\bar{L}}\right)^2 \left(1 - 2e^{-4v^2-2I_0}\right)\left(1 - 4v^2\right), \tag{4.6.9}$$

$$g(v,r) = 8\left(\frac{L_r}{\bar{L}}\right)^2 vr\left(2e^{-2v^2+2I_0}\sqrt{1 - e^{-4v^2-2I_0}}\right). \tag{4.6.10}$$

Note that, in order to obtain a solution for η, we must first determine a numerical solution for $v(r)$ and, consequently, also for $f(r)$ and $g(r)$. The numerical solutions of these functions are shown in Figs. 4.6.1 and 4.6.2. On the other hand, for $I_0 \leq 1$, we find that $v(r) \approx r$, and as I_0 becomes smaller the solution enters a linear regime. This is consistent with the fact that small values of I_0 correspond to the low–energy regime and, therefore, to a strongly interacting regime.

4.6.1 The Maxwell equations

The perturbation induced by the external magnetic field b_e also affects the Maxwell equation (2.2.6), which represents the field equation for the function $v(r)$. In this case, an external current J_e must be introduced so that it contributes as follows

$$\hat{v}'' - 4KL_r^2 \sin^2(\hat{H})\hat{v} = J_e, \tag{4.6.11}$$

where $\hat{v}(r) = v(r) + b_e r$ and $\hat{H}(r) = H(r) + b_e\eta(r)$ are the perturbed fields. At first order on the perturbation b_e, (4.6.11) becomes

$$J_e = \left[v'' - 4KL_r^2 \sin^2(H)v\right] - 4b_eKL_r^2\left(r\sin^2 H + \eta v \sin(2H)\right). \tag{4.6.12}$$

The term in square brackets, which is independent of b_e, is identically zero as a consequence of the field equation (2.2.6). Hence, the external current takes the form

$$J_e = -4b_eKL_r^2\left(r\sin^2 H + \eta v \sin(2H)\right). \tag{4.6.13}$$

4.6.2 Contribution to the energy density and total energy

Using the results discussed above, we can compute the energy density (2.2.7) to first order in the external magnetic field perturbation, obtaining

$$\begin{aligned} T_{00}^{b_e} = T_{00} + b_e\Bigg[&\frac{8K}{\bar{L}^2}vr\sin^2 H \\ &+\frac{4K}{\bar{L}^2}\eta\left(v^2 - \frac{1}{4}\right)\sin(2H) + \frac{K}{L_r^2}\eta' H' + \frac{2v'}{(L_r\bar{L})^2}\Bigg]. \end{aligned} \tag{4.6.14}$$

By making use of the field equations (2.2.5) and (2.2.6), the perturbed energy density $T_{00}^{b_e}$ can be expressed as

$$T_{00}^{b_e} = T_{00} + \frac{b_e}{L_r^2}\frac{d}{dr}\left(\frac{2v'r}{\bar{L}^2} + K\eta H'\right). \tag{4.6.15}$$

In this way, the contribution of the external field to the energy density can be written as a total derivative. The derivatives of the fields H' and v' are replaced using the BPS equations (3.3.8) and (3.3.9), together with the condition (3.3.3). Explicitly, we obtain

$$T_{00}^{b_e} = T_{00} + \frac{4K^{\frac{3}{2}}b_e}{L_r}\frac{d}{dr}\left(r\cos H - v\eta\sin H\right). \tag{4.6.16}$$

Using this energy density, we can compute the total energy, including the effects of the external field b_e, by integrating (4.6.16) over the volume of the layers

$$E_{b_e} = E + b_e\delta E, \tag{4.6.17}$$

where

$$\delta E = 8\pi^3 K^{\frac{1}{2}}\cos H(2\pi) - 9\pi^2 p^2 K^{\frac{1}{2}} v(2\pi)\eta(2\pi)\sin H(2\pi). \tag{4.6.18}$$

The contribution of the external magnetic field b_e to the total energy can be written in terms of the magnetic flux Φ and the integration constant I_0, using the BPS relation (3.3.12) together with Eq. (3.3.16). In this way, we can obtain a relation between the magnetic flux Φ and I_0, as was done previously when solving the integral (3.3.14) numerically, or by considering its analytic approximation (3.6.4), in order to determine this relation explicitly. On the other hand, we must specify the boundary conditions for $\eta(2\pi)$ in order to understand the behavior of the total energy in the presence of the external magnetic field. With this in mind, we first compute the contribution of the external magnetic field to the baryonic charge.

$$B_{b_e} = B + b_e\delta B, \tag{4.6.19}$$

where

$$\delta B = -12p^2 b_e \left[4\pi(1-\sin^2(H(2\pi))) \; -4\eta(2\pi)v(2\pi)\sin(H(2\pi))\cos(H(2\pi))\right]. \tag{4.6.20}$$

The presence of the external magnetic field should not alter the value of the baryonic charge. Therefore,

$$4\pi(1-\sin^2(H(2\pi))) - 4\eta(2\pi)v(2\pi)\cos(H(2\pi)) = 0, \tag{4.6.21}$$

which solution is

$$\eta(2\pi) = \frac{\pi}{v(2\pi)}\frac{\cos(H(2\pi))}{\sin(H(2\pi))} \tag{4.6.22}$$

Using this result, we can explicitly compute the contribution to the energy (4.6.18) due to the presence of the external magnetic field, obtaining

$$\delta E = -\pi^3 p^2 K^{\frac{1}{2}} \cos(H(2\pi)). \tag{4.6.23}$$

The contribution to the total energy arising from the presence of the external magnetic field is shown in Fig. 4.6.3, where the analytic approximation (3.6.4) has been used.

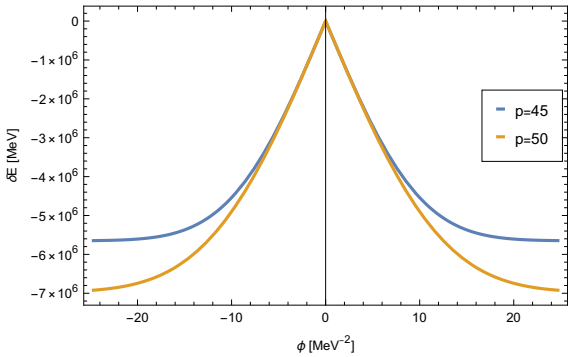

Figure 4.6.3: Contribution of the external field to the total energy as a function of the flux Φ. Here $K = 2$ fm^{-2} and $L_r = 25$ fm.

It is important to note that when the external magnetic field is positive, namely

$b_e > 0$, or equivalently when it is parallel to the magnetic field of the layers, the contribution to the energy satisfies $\delta E < 0$. This indicates that the solutions describing the magnetic layers exhibit ferromagnetic behavior.

The contribution to the free energy at first order in b_e can be written as

$$\mathcal{F}_{b_e} = \mathcal{F} + b_e np^2 \ \delta\mu_B, \tag{4.6.24}$$

where

$$\delta\mu_B = \frac{1}{np^2}\left(\delta E - L_r \frac{\partial \delta E}{\partial L_r}\right). \tag{4.6.25}$$

4.6.3 Magnetic susceptibility

With the results presented in this section, we can now compute the magnetic susceptibility analytically from the partition function, using the following expression

$$\chi = \frac{\mu_0}{\beta} \lim_{b_e \to 0} \left(\frac{\partial^2 \ln \mathcal{Z}_{b_e}}{\partial {b_e}^2} \right), \tag{4.6.26}$$

where μ_0 is the vacuum magnetic permeability and $\mathcal{Z}_{b_e}$ is the perturbed partition function, computed using the free energy $\mathcal{F}_{b_e}$ given in (4.6.24). The behavior of the magnetic susceptibility as a function of temperature is shown in Fig. 4.6.4.

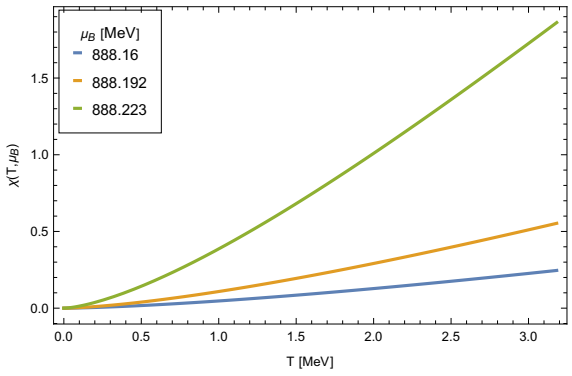

Figure 4.6.4: Magnetic susceptibility as a function of the temperature T for different values of μ_B. Here $K = 2$ fm^{-2}, $L_r = 25$ fm.

This behavior can be analyzed in more detail in the low and high temperature limits by writing the magnetic susceptibility χ explicitly as

$$\chi = \frac{\mu_0 \beta}{\pi^2 \mathcal{Z}^2} \sum_{n=1}^{n_{max}} \Big[\Delta^2(n) \Theta''(x)|_{x=\frac{\beta}{\pi} x_0(n)} \mathcal{Z} - \Delta(n) \Theta'(x)|_{x=\frac{\beta}{\pi} x_0(n)} \sum_{m=1}^{n_{max}} \Delta(m) \Theta'(x)|_{x=\frac{\beta}{\pi} x_0(m)} \Big], \tag{4.6.27}$$

where $x_0(n) = n(\mu_B^*(n) - \mu_B)$ and $\Delta(n) = n\,\delta\mu_B(n)$. In this equation, the prime denotes the derivative with respect to x. This expression is also valid in the case where n is treated as a continuous variable, in that case, the sum must be replaced by an integral.

For high temperatures (or small values of β), we use the approximation (A0.7) for $\Theta(x)$ in order to obtain

$$\chi \approx \frac{\mu_0}{4\beta} \sum_{n,m=1}^{n_{max}} \left[\frac{3\Delta^2(n)}{[x_0(n)]^{\frac{5}{2}} [x_0(m)]^{\frac{1}{2}}} - \frac{\Delta(n)\Delta(m)}{[x_0(n)]^{\frac{3}{2}} [x_0(m)]^{\frac{3}{2}}} \right] \tag{4.6.28}$$

Since $\beta = 1/(k_B T)$, then, $\chi \propto T$ in the high temperature limit.

For low temperatures (or large values of β), we can explicitly use the following expression for $\Theta(x)$

$$\Theta(x) = 1 + 2 \sum_{p=1}^{\infty} e^{-p^2 \pi x}. \tag{4.6.29}$$

Thus,

$$\frac{d}{dx}\Theta(x) = -2\pi \sum_{p=1}^{\infty} p^2 e^{-p^2 \pi x}, \tag{4.6.30}$$

and

$$\frac{d^2}{dx^2}\Theta(x) = 2\pi^2 \sum_{p=1}^{\infty} p^4 e^{-p^2 \pi x}, \tag{4.6.31}$$

where $x = \frac{\beta}{\pi} n(\mu_B^*(n) - \mu_B)$. Then, when $\beta \to \infty$, both the first and second derivative goes to zero with order $e^{-\beta}$. Moreover, $\Theta(x) \to 1$ and $\mathcal{Z}$ is a finite constant different from zero. This means that $\chi \to 0$ as $\beta \to \infty$.

Similarly, these expressions remain valid when n is considered as a continuous variable.

The increase of the magnetic susceptibility with temperature observed in Fig. 4.6.4 can be understood as follows. At low temperatures, this growing behavior may be related to the Hopkinson effect, which is characteristic of ferromagnetic and ferrimagnetic materials [76]. As the temperature approaches the Curie temperature T_c, the magnetic susceptibility is expected to begin decreasing. However, at sufficiently high temperatures the present low–energy model ceases to be applicable, and therefore the current expression for the magnetic susceptibility should only be regarded as reliable in the low–temperature regime.

Chapter 5

The Effects of the Isospin Chemical Potential

In this chapter, we expand our previous thermodynamic analysis by including the effects of the isospin chemical potential. In realistic physical scenarios, such as the interior of neutron stars, nuclear matter is highly asymmetric in its isospin content, containing a significantly larger fraction of neutrons than protons. Introducing an isospin chemical potential is essential to accurately model this asymmetry. First, in section 5.1, we derive the modified BPS bound to account for this new chemical potential. Then, in section 5.2, we study the subsequent approximations and the behavior of the topological charge. Afterwards, in sections 5.3 and 5.4, we recalculate the partition function and the macroscopic thermodynamical quantities to explicitly show their dependence on the isospin. Finally, in section 5.5, we present the modified equation of state and the speed of sound for the system with a non-zero isospin chemical potential, contrasting these results with the symmetric case.

5.1 Modified BPS bound

To introduce the asymmetry between protons and neutrons in our theory, we must include the effect of the isospin chemical potential. As has been previously studied, in the case of a field theory with internal symmetry $SU(2)$ (see, for instance [77, 78, 79, 80] and references therein), the effects of the isospin chemical potential μ_I can be introduced by modifying the covariant derivative as follows:

$$D_\mu U \to \bar{D}_\mu U = D_\mu U + \mu_I [\tau_3, U] g_{\mu 0}. \tag{5.1.1}$$

With this definition of the derivative, and considering the ansatz previously presented in (2.2.3) and (2.2.4), the energy density becomes the free energy density in the presence of the isospin chemical potential:

$$T_{00}^I = T_{00} + 2K\mu_I^2 \sin^2 H, \tag{5.1.2}$$

where T_{00} is the energy density without the effects of the isospin chemical potential (2.2.7). In this case, and for consistency, the equations of motion are now obtained by minimizing the free energy density:

$$H'' + \left(\frac{L_r}{L}\right)^2 \left(p^2 - 2L^2\mu_I^2 - 4u^2\right) \sin(2H) = 0, \tag{5.1.3}$$

$$u'' - 4uKL_r^2 \sin^2 H = 0. \tag{5.1.4}$$

Remarkably, the system with the inclusion of the isospin chemical potential still admits a BPS formulation similar to the one presented in Chapter 3. Using the Hamilton–Jacobi technique, the free energy density T_{00}^I can be written as a sum of squares plus a total derivative and a constant:

$$T_{00}^I = \frac{K}{2L_r^2}\left(H' + \frac{4L_r\sqrt{K+\mu_I^2}}{p} u \sin H\right)^2 + \frac{2(K+\mu_I^2)}{L_r^2 p^2}\left(u' - \frac{pKL_r}{\sqrt{K+\mu_I^2}} \cos H\right)^2 + \frac{dW}{dr} + 2K\mu_I^2 \tag{5.1.5}$$

where the superpotential W is the solution of the Hamilton-Jacobi equation:

$$W = \frac{4K\sqrt{K+\mu_I^2}}{pL_r} u \cos H, \tag{5.1.6}$$

and the BPS condition now requires the following quantization condition:

$$L = \frac{p}{\sqrt{2(K+\mu_I^2)}} \leftrightarrow A = \pi^2 \frac{p^2}{K+\mu_I^2}. \tag{5.1.7}$$

In this way, the free energy takes the form:

$$F_I = \int d^3x \sqrt{-g} T_{00}^I = AL_r \int_0^{2\pi} dr T_{00}^I \geq |E_I|, \tag{5.1.8}$$

where

$$E_I = \frac{AL_r}{e^2} |W(2\pi) - W(0) + 4\pi K \mu_I^2|. \tag{5.1.9}$$

With the above, the BPS equations modified by the presence of μ_I are:

$$H' + \frac{4L_r\sqrt{K+\mu_I^2}}{p} u \sin H = 0, \tag{5.1.10}$$

$$u' - \frac{pKL_r}{\sqrt{K+\mu_I^2}} \cos H = 0. \tag{5.1.11}$$

Note that, as expected, the first-order BPS equations modified by the isospin chemical potential imply the second-order field equations depending on μ_I. Similar to the case with $\mu_I = 0$, by using the BPS condition as in 3.3, the first-order equations of motion are reduced to the following quadrature:

$$2\pi\sqrt{K} L_r = \int_0^{v(2\pi)} \frac{\sqrt{\frac{K+\mu_I^2}{K}} dv}{\sqrt{1 - \exp\left(-\frac{4(K+\mu_I^2)}{K} v^2 - 2I_0\right)}}, \tag{5.1.12}$$

with $pv(r) = u(r)$ such that $v(2\pi)$ is p-independent. Similarly to the previous sections, we can write $v(2\pi)$ in terms of the magnetic flux in the y direction as follows

$$\Phi = \frac{p^2 \pi L_r}{\sqrt{2(K+\mu_I^2)}} (v(2\pi) - v(0)). \tag{5.1.13}$$

If we consider $v(0) = 0$, we can solve for $v(2\pi)$ in terms of the magnetic flux Φ

$$v(2\pi) = \frac{\sqrt{2(K+\mu_I^2)}}{p^2 \pi L_r} \Phi. \tag{5.1.14}$$

Let us note that, due to the presence of the isospin chemical potential, the magnetic flux is reduced. With the above, we can rewrite the baryonic charge B_I and the topological charge Q_I as functions of the magnetic flux and the isospin chemical potential:

$$B_I = \frac{4\sqrt{2(K+\mu_I^2)}}{\pi L_r}\Phi\mathcal{M}_\Phi, \tag{5.1.15}$$

$$E_I = \frac{4\sqrt{2}\pi K}{L_r}\Phi\sqrt{\mathcal{M}_\Phi} + \frac{4\pi^3 p^2 L_r K\mu_I^2}{K+\mu_I^2}, \tag{5.1.16}$$

where

$$\mathcal{M}_\Phi = 1 - \exp\left(-\frac{8(K+\mu_I^2)^2}{Kp^4\pi^2 L_r^2}\Phi^2 - 2I_0\right) \tag{5.1.17}$$

5.2 Approximation and topological charge

In order to obtain an analytic expression relating the topological charge, the baryonic charge, the magnetic flux, and the isospin chemical potential, we must repeat the analysis presented in 3.6 to find an analytic expression for the integration constant I_0 (5.1.12). For this purpose, it is useful to introduce the following rescaling:

$$s^2 = \frac{(K+\mu_I^2)}{K}v^2 \implies v = \sqrt{\frac{K}{K+\mu_I^2}}s. \tag{5.2.1}$$

In this way, (5.1.12) takes the following form:

$$2\pi\sqrt{K}L_r = \int_0^{s(2\pi)} \frac{ds}{\sqrt{1-e^{-4s^2-2I_0}}}. \tag{5.2.2}$$

Note that the previous expression has the same form as (3.6.1). In this way, we can use the approximations presented in 3.6 to derive an analytic expression for $v(2\pi)(I_0)$ and its inverse $I_0(v(2\pi))$:

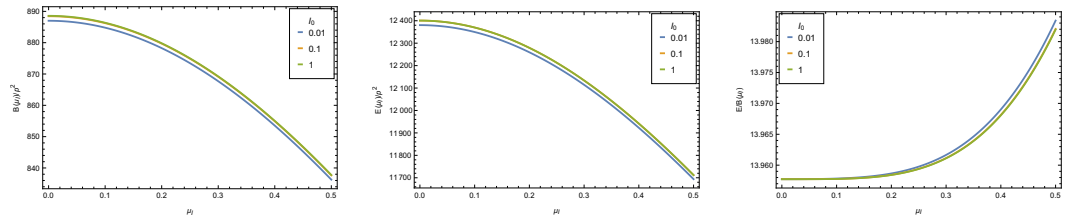

(a) **(b)** **(c)**

Figure 5.2.1: Baryonic charge (Fig. 5.2.1a), total energy (Fig. 5.2.1b) and energy per baryon (Fig. 5.2.1c) in terms of μ_I. Here $K = 2$ fm^{-2}, $L_r = 25$ fm.

$$s(2\pi) = \sqrt{\frac{K+\mu_I^2}{K}} v(2\pi) \approx \begin{cases} \left[2\pi\sqrt{K}L_r + \frac{1}{4}\ln\left(1 - e^{-2I_0}\right)\right] & \text{for } I_0 \geq \varepsilon, \\ \sqrt{\frac{I_0}{2}}\sinh(4\pi\sqrt{K}L_r) & \text{for } I_0 < \varepsilon, \end{cases} \tag{5.2.3}$$

$$I_0 \approx \begin{cases} -\frac{1}{2}\log\left[1 - \exp\left(4\sqrt{\frac{K+\mu_I^2}{K}}v(2\pi) - 8\pi\sqrt{K}L_r\right)\right] & \text{for } \sqrt{\frac{K+\mu_I^2}{K}}v(2\pi) \geq \tilde{\varepsilon}, \\ \frac{K+\mu_I^2}{K}v^2(2\pi)\frac{2}{\sinh^2(4\pi\sqrt{K}L_r)} & \text{for } \sqrt{\frac{K+\mu_I^2}{K}}v(2\pi) < \tilde{\varepsilon}. \end{cases} \tag{5.2.4}$$

This allows us to define the baryonic charge B_I and the topological charge (energy) E_I in terms of $v(2\pi)$ and the isospin chemical potential μ_I,

$$B_I = 4p^2 v(2\pi)\ \mathcal{M}, \tag{5.2.5}$$

$$E_I = \frac{4\pi^2 p^2 K}{\sqrt{K+\mu_I^2}} v(2\pi)\ \mathcal{M} + \frac{4\pi^3 p^2 L_r K \mu_I^2}{K+\mu_I^2}, \tag{5.2.6}$$

where

$$\mathcal{M} = 1 - e^{-\frac{4(K+\mu_I^2)}{K}v^2(2\pi) - 2I_0}. \tag{5.2.7}$$

Figure 5.2.1 shows the topological charge, the energy, and the energy per baryon.

5.3 The partition function and its dependence on the chemical potential

Similar to the case without the isospin chemical potential, we define n as follows:

$$n = \frac{B_I}{p^2}, \tag{5.3.1}$$

where n is considered as a continuous quantity, motivated by the observations outlined in the section 4.3.

As in the case with vanishing isospin chemical potential, the quantity n converges to a finite value when $I_0 \to \infty$, which in this case depends on μ_I

$$n_{max}(\mu_I) = \lim_{I=\to+\infty} \frac{B_I}{p^2} = \frac{8\pi K L_r}{\sqrt{K+\mu_I^2}}. \tag{5.3.2}$$

Note that we can also derive a maximum value for the magnetic flux directly by using the approximation for I_0 given in (5.2.4):

$$\Phi_{max} = \frac{\sqrt{2}\pi^2 p^2 K L_r^2}{K+\mu_I^2}. \tag{5.3.3}$$

It is worth emphasizing that, due to the presence of the isospin chemical potential, the value of $n_{\max}$ decreases due to its effect, as can be seen in Fig. 5.3.1.

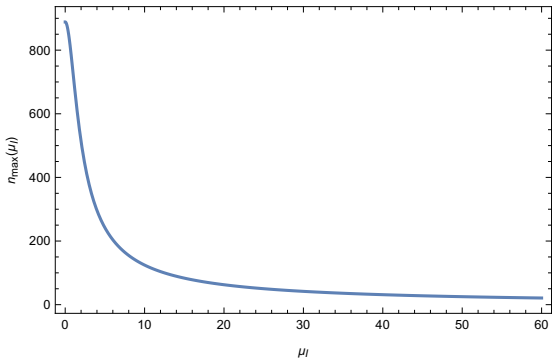

Figure 5.3.1: n_{max} as a function of μ_I. Here $K = 2$ fm^{-2}, $L_r = 25$ fm.

With all the above, we can compute the grand canonical partition function, including the effects of μ_I, as follows:

$$\mathcal{Z}(\beta,\mu_B,\mu_I)=\iint\sum_{p=-\infty}^{+\infty}e^{-\beta p^2\mathcal{F}_I(n,\mu_B,\mu_I)}\,dn\,dn_I. \tag{5.3.4}$$

where

$$\mathcal{F}_I(n,\mu_B,\mu_I)=G_I-n\mu_B-n_I\mu_I, \tag{5.3.5}$$

and n_I is the isospin number. As we will see later in this chapter, n_I is not an independent quantity, but rather depends on n. In this way, the double integral in the definition of the partition function (5.3.4) becomes a single integral such that $n\in(0,n_{max}(\mu_I)]$.

On the other hand using equations (5.1.15) and (5.1.16) we obtain that,

$$G_I=\frac{2\pi^2K}{\sqrt{K+\mu_I^2}}\sqrt{nv(2\pi)(n,\mu_I)}+\frac{4\pi^3KL_r\mu_I^2}{K+\mu_I^2}. \tag{5.3.6}$$

We must analyze the free energy in depth in order to understand the behavior of the partition function. To this end, we first note that the quantity n_I corresponds to the isospin charge, defined as follows:

$$Q_I=\int d^3xJ_0^3, \tag{5.3.7}$$

where J_0^3 is the 0 component along τ_3 of the isospin current

$$J_\mu^a=2K\mathrm{Tr}\left(D_\mu UU^{-1}\tau^a\right), \tag{5.3.8}$$

and D_μ is the usual covariant derivative. In this way, we obtain the following expression for the isospin charge:

$$Q_I=\frac{8KL_r\mu_I\pi^2p^2}{K+\mu_I^2}\int dr\sin^2H, \tag{5.3.9}$$

which also corresponds to the volume integral of the component of the energy density (5.1.2) associated with the isospin chemical potential. By using the BPS

equations, we can rewrite the isospin charge in terms of $v(r)$ as follows:

$$Q_I = \frac{8\mu_I\sqrt{K}\pi^2 p^2}{K+\mu_I^2}\,\mathcal{I}, \tag{5.3.10}$$

where

$$\mathcal{I} = \int_0^{\sqrt{\frac{K+\mu_I^2}{K}}v(2\pi)} \frac{e^{-4x^2-2I_0}}{\sqrt{1-e^{-4x^2-2I_0}}}dx. \tag{5.3.11}$$

The numerical solution to the integral (5.3.11) is graphically represented in Fig. 5.3.2.

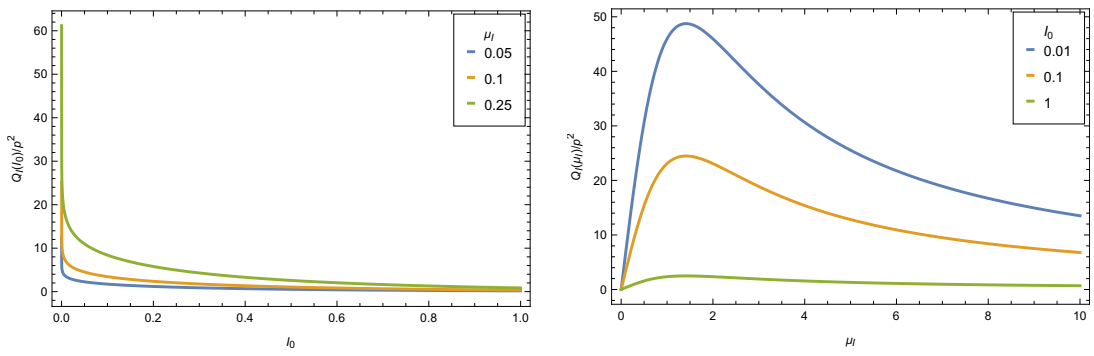

(a) **(b)**

Figure 5.3.2: Behavior of Q_I/p^2 as a function of I_0 for different values of μ_I (Fig. 5.3.2a), and as a function of μ_I (Fig. 5.3.2b). Here $K = 2$ fm^{-2} and $L_r = 25$ fm. Note that Q_I reaches a maximum for a specific value of μ_I and then tends to zero for large values of μ_I. This behavior is due to the decrease in the total number of baryons, as shown in (Fig. 5.2.1).

As we mentioned before, the isospin charge Q_I, and therefore n_I, is not an independent quantity, but rather depends on the baryonic charge. In particular, using the relation (5.1.15), we can rewrite I_0 in terms of n and substitute this expression into (5.2.5). In this way, the double integral in the partition function reduces to a single integral over n.

Let us observe that the ratio between the isospin charge Q_I and the baryonic charge B_I is determined by

$$\frac{Q_I}{B_I} = \frac{2\pi^2\sqrt{K}\mu_I}{(K+\mu_I^2)v(2\pi)\,\mathcal{M}}\,\mathcal{I}, \tag{5.3.12}$$

where $\mathcal{M}$ and $\mathcal{I}$ were defined previously in (5.2.7) and (5.3.11), respectively. In Fig. 5.3.3, this ratio is shown numerically. We can observe that, once the boundary conditions in the solution for $H(r)$ are fixed and with I_0 fixed, the ratio (5.3.12), for large values of the isospin chemical potential, becomes constant.

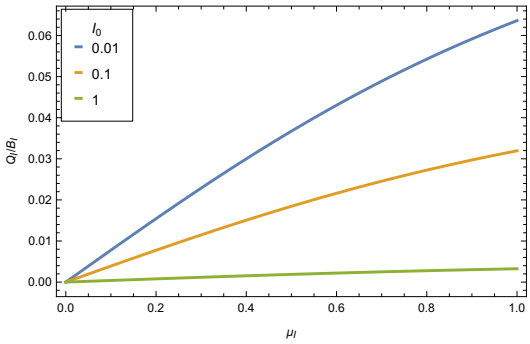

Figure 5.3.3: The ratio Q_I/B_I as a function of μ_I. Here $K = 2\ \text{fm}^{-2}$, $L_r = 25\ \text{fm}$.

It is possible to obtain a good approximation for the integral (5.3.11) by using the approximations presented in Appendix A. When I_0 is not too small, that is, for $I_0 > \epsilon$, we can consider the following approximation:

$$\mathcal{I} \approx \frac{1}{8}\left[Li_2\left(e^{-2I_0}\right) - 2\log\left(1 - e^{-2I_0}\right)\right]. \tag{5.3.13}$$

On the other hand, for the case $I_0 \leq \epsilon$, which means that $\frac{K+\mu_I^2}{K}v^2(2\pi)$ is also small (see equation (5.2.3)), we consider the following approximation:

$$\begin{aligned}\mathcal{I} \approx \frac{1}{4}\Bigg[&\ln\left(1 + x + \sqrt{x(2+x)}\right) \\ &- \frac{\frac{K+\mu_I^2}{K}v^2(2\pi)}{x}\left(\sqrt{(1+x)x} + \arcsin(\sqrt{x})\right)\Bigg],\end{aligned} \tag{5.3.14}$$

where $x = \frac{K+\mu_I^2}{K}\frac{4v^2(2\pi)}{I_0}$. The comparison between the numerical solution and the analytic approximations is shown in Fig. 5.3.4.

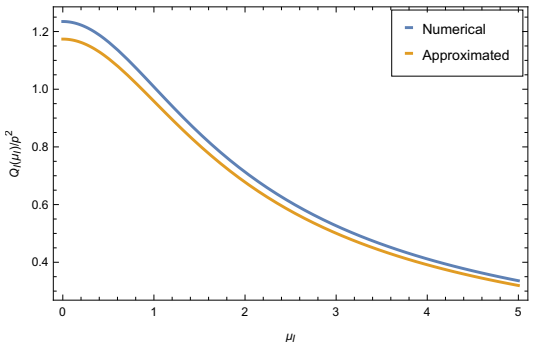

Figure 5.3.4: Comparison between the analytic approximation and the numerical integration of (5.3.11) as a function of μ_I. Here $K = 2$ fm^{-2}, $L_r = 25$ fm and $I_0 = 0.1$. The term $v(2\pi)$ is given by equation (5.2.3).

In this way, we define:

$$\alpha(n,\mu_I) = \frac{Q_I}{B_I} = \frac{\pi^2\mu_I}{4v(2\pi)(n,\mu_I)}\frac{\sqrt{K}}{K+\mu_I^2}\,\hat{\mathcal{I}}(n,\mu_I), \tag{5.3.15}$$

where $\hat{\mathcal{I}}$ takes different approximations depending on the value of I_0. For $I_0 \leq \epsilon$:

$$\hat{\mathcal{I}}(n,\mu_I) = \frac{A + \frac{K+\mu_I^2}{K}v(2\pi)^2(n,\mu_I)B}{\frac{K+\mu_I^2}{K}v(2\pi)^2(n,\mu_I)\left(1+\frac{1}{\sinh^2(4\pi\sqrt{K}L_r)}\right)} \tag{5.3.16}$$

where

$$A = \frac{1}{2}\ln\Big[\cosh^2(4\pi\sqrt{K}L_r) + \sinh(4\pi\sqrt{K}L_r)\sqrt{1+\cosh^2(4\pi\sqrt{K}L_r)}\Big], \tag{5.3.17}$$

$$B = -\frac{\cosh(4\pi\sqrt{K}L_r)}{\sinh(4\pi\sqrt{K}L_r)} - \frac{4\pi\sqrt{K}L_r}{\sinh^2(4\pi\sqrt{K}L_r)} \tag{5.3.18}$$

And for $I_0 > \epsilon$:

$$\hat{\mathcal{I}}(n,\mu_I) = \frac{Li_2\left(e^{-2I_0(n,\mu_I)}\right) - 2\log\left(1-e^{-2I_0(n,\mu_I)}\right)}{1-e^{-4\frac{K+\mu_I^2}{K}v(2\pi)^2(n,\mu_I)-2I_0(n,\mu_I)}}. \tag{5.3.19}$$

The dependence of $v(2\pi)$ and I_0 as functions of n and μ_I has been defined by imposing the condition (5.3.1) and using the relations (5.2.3) and (5.2.4). In this way, we can write the free energy as

$$\mathcal{F}_I(n, \mu_B, \mu_I) = n[\mu^*(n, \mu_I) - \mu_B - \alpha(n, \mu_I)\mu_I)], \tag{5.3.20}$$

where $\mu^*(\mu_I, n) = G_I(\mu_I, n)/n$.

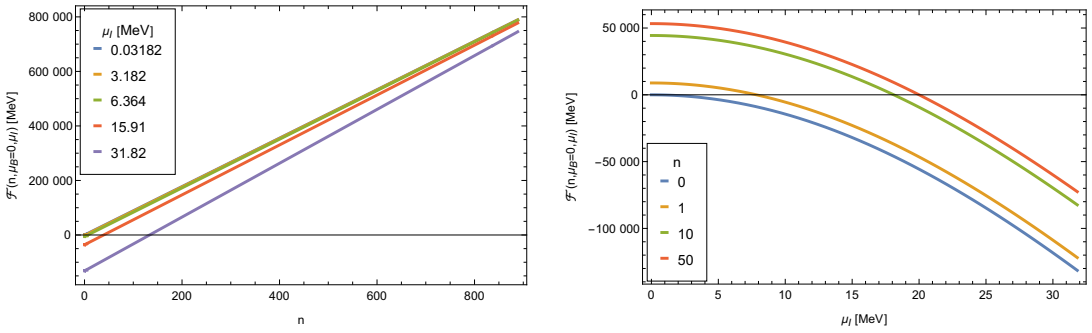

(a) **(b)**

Figure 5.3.5: Free energy as a function of n and μ_I for different values of μ_I (Fig. 5.3.5a)and n (Fig. 5.3.5b). Here $K = 2$ fm^{-2}, $L_r = 25$ fm and $\mu_B = 0$.

As in the case with vanishing isospin chemical potential, in order to obtain a well-defined partition function, the free energy must be positive. We can study the sign of the free energy in terms of μ_B, μ_I, and $\hat{n}$ through the following observations.

We begin by setting $\mu_B = 0$. Recall that our previous approximation holds for two different ranges of I_0, which correspond to two different ranges of $\hat{n} = \sqrt{\frac{K+\mu_I^2}{K}}n$ (see equations (5.2.3) and 5.2.4). Consequently, we should analyze the free energy in terms of $(\hat{n}, \mu_I)$ rather than (n, μ_I). This relationship is shown in Fig. 5.3.5. Specifically, the plot in Fig. 5.3.5a shows that $\mathcal{F}(\hat{n}, 0, \mu_I)$ is mostly linear with respect to $\hat{n}$. Therefore, we can apply the same linear approximation used for the $\mu_I = 0$ case. In this limit, the free energy expression becomes:

$$\begin{aligned}\mathcal{F}(\hat{n}, 0, \mu_I) \approx \frac{\pi^2\sqrt{K}}{K+\mu_I^2}\left(K + 3\mu_I^2\right)\hat{n} \\ - \frac{20\pi^3\mu_I^2 K L_r}{K+\mu_I^2}.\end{aligned} \tag{5.3.21}$$

As we can see in 5.3.5, both plots show that for certain values of $\hat{n}$ and μ_I, the free energy becomes negative. Using the linear approximation, we observe that in

order to avoid this problem, $\hat{n}$ must satisfy

$$\hat{n} \geq \frac{\mu_I^2}{K+3\mu_I^2} 20\pi\sqrt{K}L_r. \tag{5.3.22}$$

From this, we can note that for each μ_I there exists a lower bound for $\hat{n}$. This bound is zero only when $\mu_I = 0$. This situation is represented in the plots of Fig. 5.3.5.

Considering the previous analysis, the partition function takes the following form when $\mu_B = 0$:

$$\mathcal{Z}(\beta, 0, \mu_I) = \sqrt{\frac{K}{K+\mu_I^2}} \int_{\hat{n}_{min}(\mu_I)}^{\hat{n}_{max}} \xi\left(\frac{i\beta}{\pi}\mathcal{F}(\hat{n}, 0, \mu_I)\right)\, d\hat{n}, \tag{5.3.23}$$

where $\hat{n}_{min}(\mu_I) = \frac{\mu_I^2}{K+2\mu_I^2}(1 + 12\sqrt{K}L_r)$, $\hat{n}_{max} = 8\pi\sqrt{K}L_r$.

For the case when $\mu_B \neq 0$, the free energy is given by

$$\mathcal{F}(\hat{n}, \mu_B, \mu_I) \approx \frac{\pi^2\sqrt{K}}{K+\mu_I^2}\left[\left(K + 3\mu_I^2 - \frac{\sqrt{K+\mu_I^2}}{\pi^2}\mu_B\right)\hat{n} - 20\mu_I^2\pi\sqrt{K}L_r\right]. \tag{5.3.24}$$

Hence, the inclusion of the baryonic chemical potential also affects the range of n, leading to

$$\hat{n}_{min}(\mu_B, \mu_I) = \frac{20\pi\sqrt{K}L_r\mu_I^2}{K + 3\mu_I^2 - \frac{\sqrt{K+\mu_I^2}}{\pi^2}\mu_B}. \tag{5.3.25}$$

This leaves us with an upper bound for μ_B. Indeed, it can be seen from (5.3.24) that μ_B must satisfy

$$\mu_B \leq \pi^2 \frac{K + 3\mu_I^2}{\sqrt{K+\mu_I^2}} \equiv \tilde{\mu}_B(\mu_I). \tag{5.3.26}$$

Additionally, another necessary condition is $\hat{n}_{max} - \hat{n}_{min}(\mu_B, \mu_I) \geq 0$. This is obtained when

$$\mu_B \leq \tilde{\mu}_B(\mu_I) - \frac{5\mu_I^2\pi^2}{2\sqrt{K+\mu_I^2}}, \tag{5.3.27}$$

which is smaller than $\tilde{\mu}_B(\mu_I)$. When $\hat{n}_{min}(\mu_B, \mu_I)$ approaches $\hat{n}_{max}$, then the partition function approaches to zero.

A representation of the partition function in terms of T and μ_B, for different values of μ_I, is shown in Fig. 5.3.6.

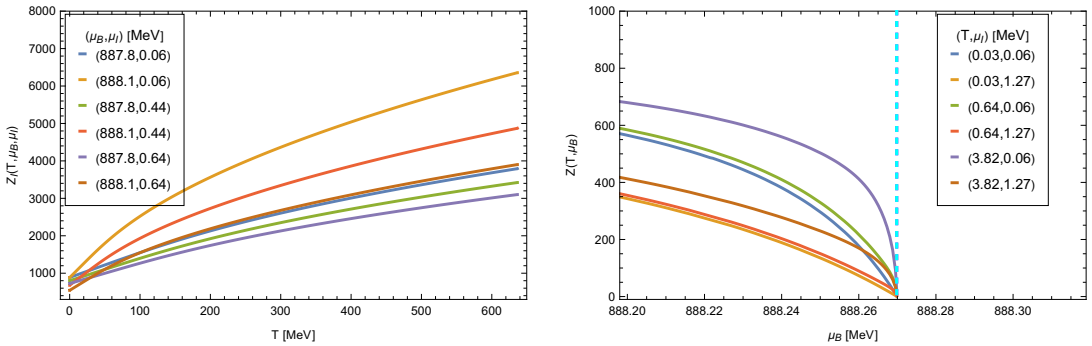

(a) **(b)**

Figure 5.3.6: Partition function as a function of T and μ_B for different values of μ_B (Fig. 5.3.6a), T (Fig. 5.3.6b) and μ_I. Here $K = 2$ fm^{-2} and $L_r = 25$ fm.

The physical interpretation of this behavior is not immediately clear. However, it is important to recall that providing an analytical description of isospin in strongly coupled systems of baryonic crystals is generally a challenging problem. Therefore, the present analysis should be regarded as an indication of a possible direction for further investigation.

5.4 Thermodynamical quantities

In this section, we analyze the same thermodynamic quantities as in Section 4.4 (namely, the average number of baryons, the heat capacity, the internal energy, and the entropy). These thermodynamic quantities are shown in Figs. 5.4.1 and 5.4.2. It is straightforward to see that for $\mu_I = 0$ we recover the same expression for the free energy. Therefore, we will focus only on the cases with $\mu_I \neq 0$.

As can be seen in Fig. 5.4.1, regarding the behavior of the average number of baryons, it is clear that the temperature required for the creation of baryons increases with the isospin chemical potential μ_I. On the other hand, as was observed in the previous analysis with $\mu_I = 0$, as μ_B increases, the temperature T required for the creation of baryons decreases.

The behavior of the remaining thermodynamic quantities as functions of μ_I is particularly interesting. In fact, we observe that nuclear matter tends to condense as μ_I increases. As shown in Figs. 5.4.2b and 5.4.2d, both the heat capacity and the internal energy decrease, eventually reaching negative and therefore non-physical values. This behavior may signal the presence of a phase transition that lies beyond the regime captured by our model.

Finally, it can be seen from the entropy plot (Fig. 5.4.2), when considered as a function of temperature, that it exhibits the same behavior as in the case with vanishing isospin chemical potential. That is, when $T \to 0$, the entropy takes a positive value different from 0. In this case, this value depends on the isospin chemical potential μ_I.

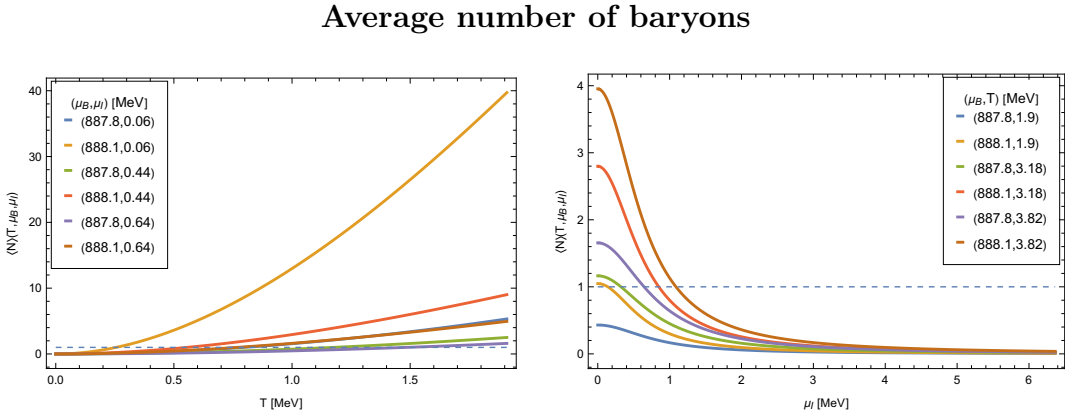

(a) **(b)**

Figure 5.4.1: Average number of baryons as a function of T and μ_I for different values of μ_I (Fig. 5.4.1a), T (Fig. 5.4.2a) and μ_B. Here $K = 2$ fm^{-2} and $L_r = 25$ fm.

5.5 Equation of state and speed of sound with non-zero isospin chemical potential

The effects of the isospin chemical potential coupled to the G-NLSM, and additionally subject to the BPS condition of the magnetized baryonic layers, modify the structure of the energy–momentum tensor, which in this case reads

$$T^{\mu}{}_{\nu} = \begin{pmatrix} -\epsilon & 0 & -L^2C & L^2C \\ 0 & T_1 & 0 & 0 \\ C & 0 & T_2 & D \\ -C & 0 & D & T_3 \end{pmatrix}, \tag{5.5.1}$$

where

$$\begin{aligned} \epsilon = {} & 2K\mu_I^2 \sin^2 H + \frac{K}{L^2}\left[p^2\cos^2(H) + 4\sin^2(H)u^2\right] \\ & + \frac{K(H')^2}{2L_r^2} + \frac{(u')^2}{(L_r L)^2} \end{aligned} \tag{5.5.2}$$

$$\begin{aligned} T_1 = {} & -2K\mu_I^2 \sin^2 H - \frac{K\left(p^2\cos^2 H + 4u^2\sin^2 H\right)}{L^2} \\ & + \frac{K(H')^2}{2L_r^2} + \frac{(u')^2}{L_r^2 L^2}, \end{aligned} \tag{5.5.3}$$

$$T_2 = T_3 = -2K\mu_I^2 \sin^2 H - \frac{K(H')^2}{2L_r^2}, \tag{5.5.4}$$

$$D = \frac{K}{L^2}\left(p^2\cos^2 H - 4u^2\sin^2 H\right) - \frac{(u')^2}{L_r^2 L^2}, \tag{5.5.5}$$

$$C = \frac{4K\mu_I}{L^2} u \sin^2 H. \tag{5.5.6}$$

Using the BPS conditions and then diagonalizing the tensor, we obtain that it takes the following form in its matrix representation:

$$(T^{\mathrm{D}})^{\mu}{}_{\nu} = \begin{pmatrix} -\frac{\epsilon}{2} + \sqrt{\Omega} & 0 & 0 & 0 \\ 0 & 0 & 0 & 0 \\ 0 & 0 & T_2 + D & 0 \\ 0 & 0 & 0 & -\frac{\epsilon}{2} - \sqrt{\Omega} \end{pmatrix}, \tag{5.5.7}$$

where $\Omega = \frac{\epsilon^2}{4} - 2L^2C^2$. Finally, by taking the trace of the energy–momentum tensor, we obtain that the pressure can be written as $P = \frac{1}{3}(T_2 + D)$. In this way,

both the pressure P and the energy density ϵ can be written as functions of the profile $v(r)$ as follows:

$$\epsilon(v,\mu_I) = 4K^2\left[1+e^{-\frac{4(K+\mu_I^2)}{K}v^2-2I_0}\left(\frac{4(K+\mu_I^2)}{K}v^2-1\right)\right] + 2K\mu_I^2, \tag{5.5.8}$$

$$P(v,\mu_I) = \frac{2K^2}{3}\left(\frac{\mu_I^2}{K+\mu_I^2} - 8v^2 e^{-\frac{4(K+\mu_I^2)v^2}{K}-2I_0}\right). \tag{5.5.9}$$

As in the case with vanishing isospin chemical potential, the energy density can be inverted, yielding the following expression

$$v(\epsilon) = \pm\sqrt{\frac{K}{4(k+\mu_I^2)}}\sqrt{1-W_0\left[\left(1+\frac{\mu_I^2}{2K}-\frac{\epsilon}{4K^2}\right)e^{1+2I_0}\right]}. \tag{5.5.10}$$

In this way, the pressure can be written in terms of ϵ:

$$P(\epsilon) = \frac{4}{3}K^2\left(1+\frac{\mu_I^2}{2K}-\frac{\epsilon}{4K^2}\right) - \frac{4}{3}K^2 e^{-1-2I_0+W_0\left[\left(1+\frac{\mu_I^2}{2K}-\frac{\epsilon}{4K^2}\right)e^{1+2I_0}\right]}. \tag{5.5.11}$$

The representation of the pressure in terms of the energy density for different values of μ_I is given in Fig. 5.5.1. Note that, at low energies, there exists a region in which the pressure is positive (in contrast to the case without isospin chemical potential). From this, we can say that the isospin chemical potential has the effect of stabilizing the system at low energies.

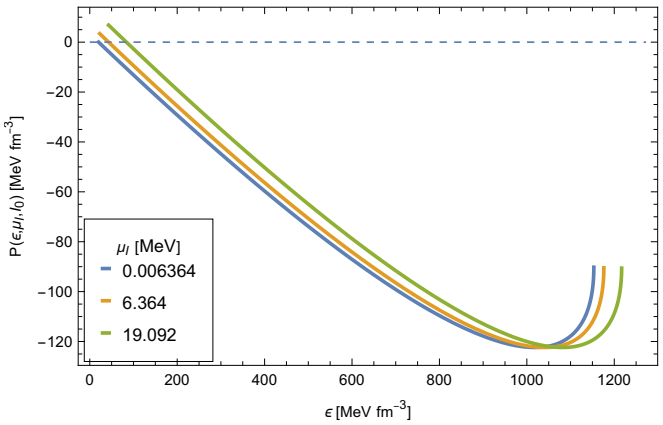

Figure 5.5.1: Pressure as a function of ϵ for different values of μ_I. Here $K = 2$ fm^{-2}, $L_r = 25$ fm, $I_0 = 0.01$.

The speed of sound c_s^2, defined as the derivative of the pressure with respect to the energy density, finally takes the form

$$c_s^2 = \frac{\partial P}{\partial \epsilon} = \frac{1}{3}\left(\frac{1}{1+W_0\left[\left(1+\frac{\mu_I^2}{2K}-\frac{\epsilon}{4K^2}\right)e^{1+2I_0}\right]}-1\right), \tag{5.5.12}$$

which is represented in Fig. 5.5.2.

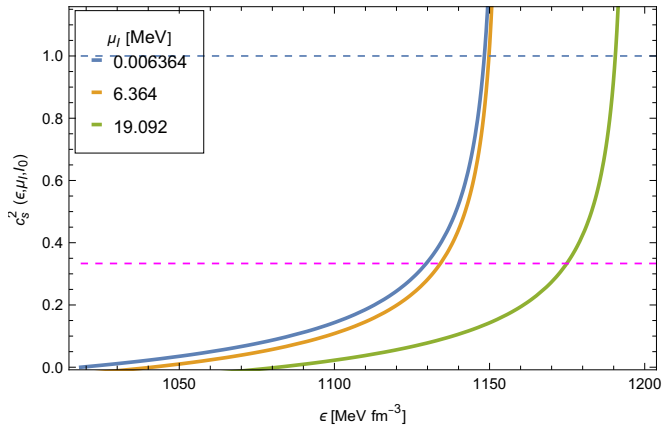

Figure 5.5.2: Speed of sound as a function of ϵ for different values of μ_I. Here $K = 2$ fm^{-2}, $L_r = 25$ fm, $I_0 = 0.01$. The magenta line represents the conformal limit $c_s^2 = \frac{1}{3}$. The values of ϵ for which $c_s^2 > 1$ are not physical and are associated with the use of the Lambert function.

In the limit $\mu_I \to 0$, the expressions for $\epsilon(v)$ and $P(v)$ consistently recover the results presented in Section 4.5. Consequently, the observations discussed there for the case $\mu_I = 0$ remain valid also in the present case.

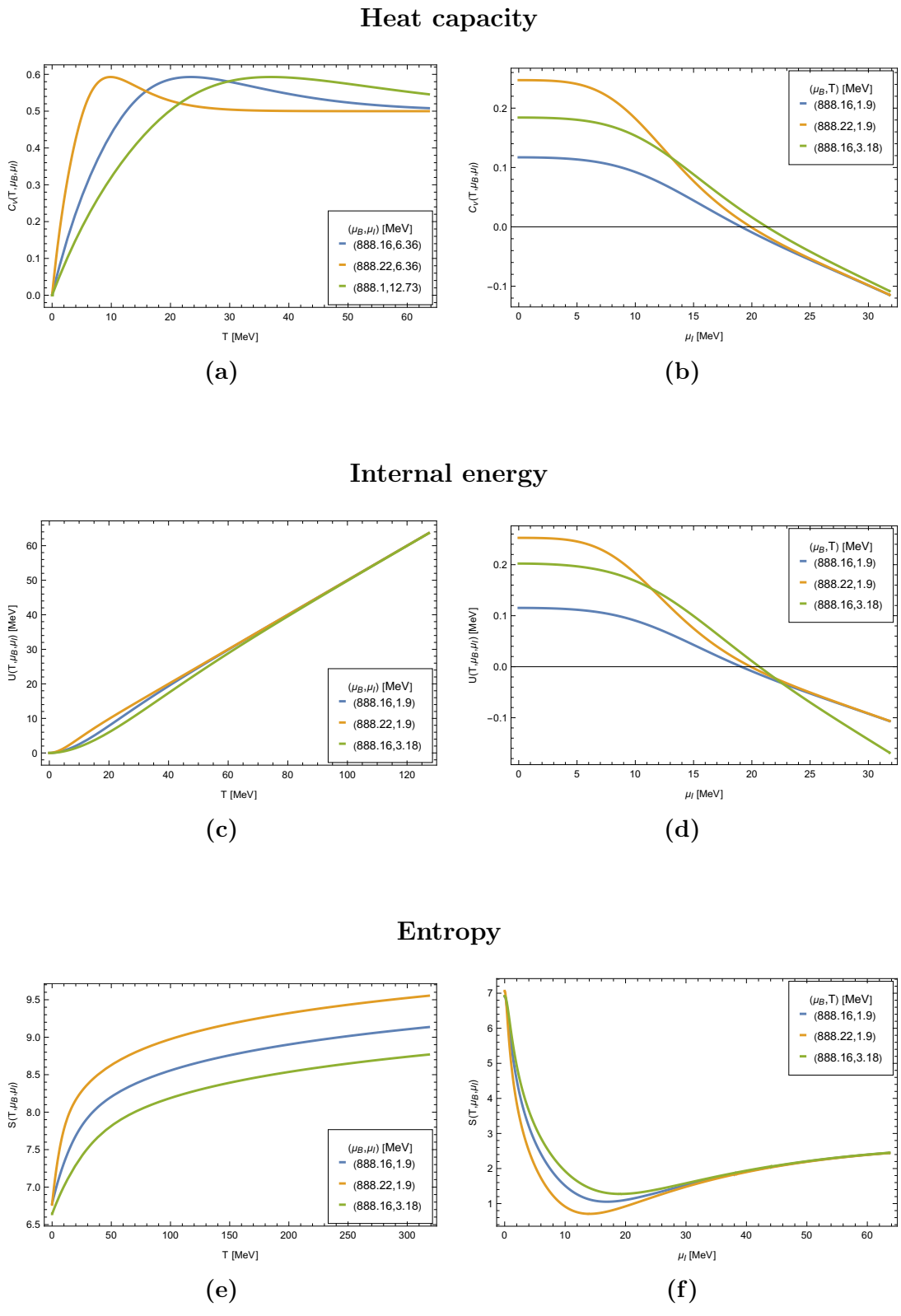

Figure 5.4.2: Thermodynamical quantities as functions of T and μ_I. Here $K = 2$ fm^{-2}, $L_r = 25$ fm.

Chapter 6

Conclusion

In the present thesis, we have analyzed the semiclassical thermodynamics of magnetized BPS baryonic layers in the nonlinear sigma model minimally coupled to Maxwell theory (G-NLSM), which possess both baryonic charge and magnetic flux. For the mathematical construction of these layers, we have utilized tools from the Hamilton-Jacobi equation of classical mechanics and BPS soliton theory. The G-NLSM describes the low-energy limit of quantum chromodynamics (QCD), which also includes the electromagnetic interactions of the hadronic degrees of freedom. In the case where the isospin chemical potential vanishes, the topological charge, which plays the role of the energy of these layers and appears naturally on the right-hand side of the BPS bound, is a nonlinear function of the baryonic charge. Due to this, and given that it is a strongly interacting system, the analysis of the thermodynamics of magnetized baryonic layers proves highly non-trivial. Using techniques from Casimir effect theory, we were able to calculate an analytical relationship between the topological charge, the baryonic charge, and the magnetic flux, thus achieving the construction of the grand canonical partition function, which is interestingly related to the Riemann zeta function. With this, we have been able to analytically obtain various thermodynamic quantities such as the internal energy, entropy, heat capacity, and magnetic susceptibility of these layers. Remarkably, this analysis can be extended to include the effects of the isospin chemical potential, which is essential for the description of nuclear pasta phases. We have explicitly constructed the BPS bound and its corresponding BPS configurations by introducing the effects of the isospin chemical potential. The topological charge that naturally appears on the right-hand side of the BPS

bound (which is also a nonlinear function of the baryonic charge), in this case, takes the role of the free energy of the magnetized baryonic layers. Furthermore, we have been able to construct the equation of state analytically via the energy-momentum tensor and, using this, calculate the speed of sound for both the case where we consider the isospin chemical potential and the case where it is zero. Deriving explicit thermodynamic expressions at finite baryonic density for a strongly interacting magnetized system is a non-trivial achievement, especially taking into account the lattice QCD sign problem at finite baryonic density. The properties of these thermodynamic quantities appear reasonable and may be useful for improving our understanding of highly interacting magnetized baryonic systems.

As a final comment, the introduction mentioned the possibility of describing nuclear pasta phases using our results, particularly the lasagna phase. However, a direct comparison of the physical quantities in this work with neutron star physics is not possible at this stage, as it requires an extension of the model. Although we were able to describe the physical properties of ordered structures of baryons organized in layers, which would constitute the solid part of the lasagna-type structures (a significant achievement, as these results are generally difficult to obtain using analytical tools), our analysis omits the contribution of liquid and gaseous nuclear matter, as well as the electron gas surrounding these layers. Omitting these contributions makes a reliable comparison with experimental data impossible. The study of these extensions will be part of future work.

Bibliography

[1] Adam Bzdak, Shinichi Esumi, Volker Koch, Jinfeng Liao, Mikhail Stephanov, and Nu Xu. Mapping the phases of quantum chromodynamics with beam energy scan. *Physics Reports*, 853:1–87, 2020.

[2] Keitaro Nagata. Finite-density lattice qcd and sign problem: Current status and open problems. *Progress in Particle and Nuclear Physics*, 127:103991, 2022.

[3] N Yu Astrakhantsev, VV Braguta, NV Kolomoyets, A Yu Kotov, DD Kuznedelev, AA Nikolaev, and A Roenko. Lattice study of qcd properties under extreme conditions: temperature, density, rotation, and magnetic field. *Physics of Particles and Nuclei*, 52:536–541, 2021.

[4] Nikita Astrakhantsev, VV Braguta, Marco Cardinali, Massimo D'Elia, Lorenzo Maio, Francesco Sanfilippo, Anton Trunin, and Artem Vasiliev. Electromagnetic conductivity of quark-gluon plasma at non-zero baryon density. *arXiv preprint arXiv:2110.10727*, 2021.

[5] Bastian Benjamin Brandt, Francesca Cuteri, Gergely Endrődi, Gergely Markó, Leon Sandbote, and Adeilton Dean Marques Valois. Thermal qcd in a non-uniform magnetic background. *Journal of high energy physics*, 2023(11):1–27, 2023.

[6] Wit Busza, Krishna Rajagopal, and Wilke Van Der Schee. Heavy ion collisions: the big picture and the big questions. *Annual Review of Nuclear and Particle Science*, 68(1):339–376, 2018.

[7] Kohsuke Yagi, Tetsuo Hatsuda, and Yasuo Miake. *Quark-gluon plasma: From big bang to little bang*, volume 23. Cambridge University Press, 2005.

[8] Claudio Oscar Dorso, Guillermo Alberto Frank, and Jorge A López. Phase transitions and symmetry energy in nuclear pasta. *Nuclear Physics A*, 978: 35–64, 2018.

[9] Claudio Oscar Dorso, A Strachan, and Guillermo Alberto Frank. The nucleonic thermal conductivity of pastas in neutron star matter. *Nuclear Physics A*, 1002:122004, 2020.

[10] Jorge A López, Claudio O Dorso, and Guillermo Frank. Properties of nuclear pastas. *Frontiers of Physics*, 16:1–55, 2021.

[11] Mateus R Pelicer, Marco Antonelli, Débora P Menezes, and Francesca Gulminelli. Anisotropic electron transport in the nuclear pasta phase. *Monthly Notices of the Royal Astronomical Society*, 521(1):743–759, 2023.

[12] Rana Nandi and Stefan Schramm. Transport properties of the nuclear pasta phase with quantum molecular dynamics. *The Astrophysical Journal*, 852(2): 135, 2018.

[13] DG Yakovlev. Electron transport through nuclear pasta in magnetized neutron stars. *Monthly Notices of the Royal Astronomical Society*, 453(1): 581–590, 2015.

[14] DG Ravenhall, CJ Pethick, and JR Wilson. Structure of matter below nuclear saturation density. *Physical Review Letters*, 50(26):2066, 1983.

[15] Masa-aki Hashimoto, Hironori Seki, and Masami Yamada. Shape of nuclei in the crust of neutron star. *Progress of theoretical physics*, 71(2):320–326, 1984.

[16] CJ Horowitz, DK Berry, CM Briggs, ME Caplan, A Cumming, and AS Schneider. Disordered nuclear pasta, magnetic field decay, and crust cooling in neutron stars. *Physical review letters*, 114(3):031102, 2015.

[17] DK Berry, ME Caplan, CJ Horowitz, Greg Huber, and AS Schneider. "parking-garage" structures in nuclear astrophysics and cellular biophysics. *Physical Review C*, 94(5):055801, 2016.

[18] A da S Schneider, Matt E Caplan, Don K Berry, and Charles J Horowitz. Domains and defects in nuclear pasta. *Physical Review C*, 98(5):055801, 2018.

[19] Matthew E Caplan, AS Schneider, and Charles J Horowitz. Elasticity of nuclear pasta. *Physical Review Letters*, 121(13):132701, 2018.

[20] Rana Nandi and Stefan Schramm. Calculation of the transport coefficients of the nuclear pasta phase. *Journal of Astrophysics and Astronomy*, 39(4):40, 2018.

[21] Zidu Lin, Matthew E Caplan, Charles J Horowitz, and Cecilia Lunardini. Fast neutrino cooling of nuclear pasta in neutron stars: Molecular dynamics simulations. *Physical Review C*, 102(4):045801, 2020.

[22] Christopher J Pethick, Zhao-Wen Zhang, and DN Kobyakov. Elastic properties of phases with nonspherical nuclei in dense matter. *Physical Review C*, 101(5):055802, 2020.

[23] Bastian Schuetrumpf, Gabriel Martínez-Pinedo, Md Afibuzzaman, and Hasan Metin Aktulga. Survey of nuclear pasta in the intermediate-density regime: Shapes and energies. *Physical Review C*, 100(4):045806, 2019.

[24] Celso C Barros Jr, Débora P Menezes, and Francesca Gulminelli. Fluctuations in the composition of nuclear pasta in symmetric nuclear matter at finite temperature. *Physical Review C*, 101(3):035211, 2020.

[25] Javier F Acevedo, Joseph Bramante, Rebecca K Leane, and Nirmal Raj. Warming nuclear pasta with dark matter: kinetic and annihilation heating of neutron star crusts. *Journal of Cosmology and Astroparticle Physics*, 2020 (03):038, 2020.

[26] Yoichiro Nambu and Giovanni Jona-Lasinio. Dynamical model of elementary particles based on an analogy with superconductivity. ii. *Physical review*, 124 (1):246, 1961.

[27] K Rajagopal and Frank Wilczek. At the frontier of particle physics/handbook of qcd. *by M. Shifman*, 4, 2001.

[28] Mark Alford, Jeffrey A Bowers, and Krishna Rajagopal. Crystalline color superconductivity. *Physical Review D*, 63(7):074016, 2001.

[29] Roberto Casalbuoni and Giuseppe Nardulli. Inhomogeneous superconductivity in condensed matter and qcd. *Reviews of Modern Physics*, 76(1):263, 2004.

[30] THR Skyrme. A new model for nuclear matter. *Proceedings of the Royal Society of London. Series A. Mathematical and Physical Sciences*, 226(1167): 521–530, 1954.

[31] THR Skyrme. Meson theory and nuclear matter. *Proceedings of the Royal Society of London. Series A. Mathematical and Physical Sciences*, 230(1181): 277–286, 1955.

[32] THR Skyrme. A non-linear theory of strong interactions. *Proceedings of the Royal Society of London. Series A. Mathematical and Physical Sciences*, 247 (1249):260–278, 1958.

[33] Tony Hilton Royle Skyrme. A non-linear field theory. *Proceedings of the Royal Society of London. Series A. Mathematical and Physical Sciences*, 260 (1300):127–138, 1961.

[34] THR Skyrme. Particle states of a quantized meson field. *Proceedings of the Royal Society of London. Series A. Mathematical and Physical Sciences*, 262 (1309):237–245, 1961.

[35] Tony Hilton Royle Skyrme. A unified field theory of mesons and baryons. *Nuclear Physics*, 31:556–569, 1962.

[36] Shouxin Chen, Yijun Li, and Yisong Yang. Exact kink solitons in skyrme crystals. *Physical Review D*, 89(2):025007, 2014.

[37] Fabrizio Canfora. Nonlinear superposition law and skyrme crystals. *Physical Review D-Particles, Fields, Gravitation, and Cosmology*, 88(6):065028, 2013.

[38] Eloy Ayón-Beato, Fabrizio Canfora, and Jorge Zanelli. Analytic self-gravitating skyrmions, cosmological bounces and ads wormholes. *Physics Letters B*, 752:201–205, 2016.

[39] L Aviles, F Canfora, N Dimakis, and D Hidalgo. Analytic topologically nontrivial solutions of the (3+ 1)-dimensional u (1) gauged skyrme model and extended duality. *Physical Review D*, 96(12):125005, 2017.

[40] Fabrizio Canfora, Marcela Lagos, Seung Hun Oh, Julio Oliva, and Aldo Vera. Analytic (3+ 1)-dimensional gauged skyrmions, heun, and whittaker-hill equations and resurgence. *Physical Review D*, 98(8):085003, 2018.

[41] F Canfora, N Dimakis, and A Paliathanasis. Analytic studies of static and transport properties of (gauged) skyrmions. *The European Physical Journal C*, 79:1–17, 2019.

[42] E Ayon-Beato, F Canfora, M Lagos, and J Oliva. Vera, a2020epjc. 80. 384a. vol. 80, issue 5. *Eur. Phys. J. C*, page 384, 2020.

[43] PD Alvarez, F Canfora, N Dimakis, and A Paliathanasis. Integrability and chemical potential in the (3+ 1)-dimensional skyrme model. *Physics Letters B*, 773:401–407, 2017.

[44] Fabrizio Canfora. Ordered arrays of baryonic tubes in the skyrme model in (3+ 1) dimensions at finite density. *The European Physical Journal C*, 78 (11):929, 2018.

[45] Fabrizio Canfora, Seung Hun Oh, and Aldo Vera. Analytic crystals of solitons in the four dimensional gauged non-linear sigma model. *The European Physical Journal C*, 79:1–10, 2019.

[46] Fabrizio Canfora, Marcela Lagos, and Aldo Vera. Crystals of superconducting baryonic tubes in the low energy limit of qcd at finite density. *The European Physical Journal C*, 80(8):697, 2020.

[47] Marco Barsanti, Stefano Bolognesi, Fabrizio Canfora, and Gianni Tallarita. Analytic baby skyrmions at finite density. *The European Physical Journal C*, 80:1–23, 2020.

[48] Fabrizio Canfora, Stefano Carignano, Marcela Lagos, Massimo Mannarelli, and Aldo Vera. Pion crystals hosting topologically stable baryons. *Physical Review D*, 103(7):076003, 2021.

[49] Fabrizio Canfora, Alex Giacomini, Marcela Lagos, Seung Hun Oh, and Aldo Vera. Gravitating superconducting solitons in the (3+ 1)-dimensional einstein gauged non-linear σ-model. *The European Physical Journal C*, 81(1):55, 2021.

[50] Fabrizio Canfora, Adolfo Cisterna, Diego Hidalgo, and Julio Oliva. Exact pp-waves,(a) ds waves, and kundt spaces in the abelian-higgs model. *Physical Review D*, 103(8):085007, 2021.

[51] Sergio L Cacciatori, Fabrizio Canfora, Marcela Lagos, Federica Muscolino, and Aldo Vera. Analytic multi-baryonic solutions in the su (n)-skyrme model at finite density. *Journal of High Energy Physics*, 2021(12):1–30, 2021.

[52] Pedro D Alvarez, Sergio L Cacciatori, Fabrizio Canfora, and Bianca L Cerchiai. Analytic su (n) skyrmions at finite baryon density. *Physical Review D*, 101 (12):125011, 2020.

[53] Sergio L Cacciatori, Fabrizio Canfora, Marcela Lagos, Federica Muscolino, and Aldo Vera. Cooking pasta with lie groups. *Nuclear Physics B*, 976: 115693, 2022.

[54] Sergio L Cacciatori, Fabrizio Canfora, and Federica Muscolino. Pearcey integrals, stokes lines and exact baryonic layers in the low energy limit of qcd. *Nuclear Physics B*, 1000:116477, 2024.

[55] Fabrizio Canfora. Magnetized baryonic layer and a novel bps bound in the gauged-non-linear-sigma-model-maxwell theory in (3+ 1)-dimensions through hamilton-jacobi equation. *Journal of High Energy Physics*, 2023(11):1–24, 2023.

[56] Fabrizio Canfora, Marcela Lagos, and Aldo Vera. Superconducting multi-vortices and a novel bps bound in chiral perturbation theory. *Journal of High Energy Physics*, 2024(10):1–31, 2024.

[57] Fabrizio Canfora and Pablo Pais. Fractional vorticity, bogomol'nyi-prasad-sommerfield systems and complex structures for the (generalized) spinor gross-pitaevskii equations. *Nucl. Phys. B*, 1017:116955, 2025.

[58] Fabrizio Canfora and Pablo Pais. A novel bps bound with a first order bps system in the $2d$ gross-pitaevskii equation. *arXiv preprint arXiv:2501.04092*, 2025.

[59] Nicholas Manton and Paul Sutcliffe. *Topological solitons*. Cambridge University Press, 2004.

[60] Sergio Luigi Cacciatori, Fabrizio Canfora, Evangelo Delgado, Federica Muscolino, and Luigi Rosa. Thermodynamics of magnetized bps baryonic layers and the effects of the isospin chemical potential. *arXiv preprint arXiv:2505.18007*, 2025.

[61] Gregory S Adkins, Chiara R Nappi, and Edward Witten. Static properties of nucleons in the skyrme model. *Nuclear Physics B*, 228(3):552–566, 1983.

[62] Stefano Bertini, Sergio L Cacciatori, and Bianca L Cerchiai. On the euler angles for su (n). *Journal of mathematical physics*, 47(4), 2006.

[63] S Cacciatori, Francesco Dalla Piazza, and ANTONIO Scotti. Compact lie groups: Euler constructions and generalized dyson conjecture. *Transactions of the American Mathematical Society*, 369(7):4709–4724, 2017.

[64] Todd Tilma and ECG Sudarshan. Generalized euler angle parameterization for u (n) with applications to su (n) coset volume measures. *Journal of Geometry and Physics*, 52(3):263–283, 2004.

[65] Erick J Weinberg. *Classical solutions in quantum field theory: Solitons and Instantons in High Energy Physics*. Cambridge University Press, 2012.

[66] Michael Bordag, Galina Leonidovna Klimchitskaya, Umar Mohideen, and Vladimir Mikhaylovich Mostepanenko. *Advances in the Casimir effect*, volume 145. OUP Oxford, 2009.

[67] Edmund Taylor Whittaker and George Neville Watson. *A course of modern analysis*. Courier Dover Publications, 2020.

[68] Cheng-Jun Xia, Toshiki Maruyama, Nobutoshi Yasutake, and Toshitaka Tatsumi. Nuclear pasta structures at high temperatures. *Phys. Rev. D*, 106 (6):063020, 2022. doi: 10.1103/PhysRevD.106.063020.

[69] Andreas Schmitt. Chiral pasta: Mixed phases at the chiral phase transition. *Phys. Rev. D*, 101(7):074007, 2020. doi: 10.1103/PhysRevD.101.074007.

[70] Charles Kittel and Paul McEuen. *Introduction to solid state physics*. John Wiley & Sons, 2018.

[71] M. E. Caplan, C. R. Forsman, and A. S. Schneider. Thermal Fluctuations in Nuclear Pasta. *Phys. Rev. C*, 103(5):055810, 2021. doi: 10.1103/PhysRevC.103.055810.

[72] Philipe Chomaz, Maria Colonna, and Jorgen Randrup. Nuclear spinodal fragmentation. *Phys. Rept.*, 389:263–440, 2004. doi: 10.1016/j.physrep.2003.09.006.

[73] C. O. Dorso, G. A. Frank, and J. A. López. Phase transitions and symmetry energy in nuclear pasta. *Nucl. Phys. A*, 978:35–64, 2018. doi: 10.1016/j.nuclphysa.2018.07.008.

[74] Toshiki Maruyama, Nobutoshi Yasutake, and Toshitaka Tatsumi. Pasta structures in neutrino-degenerate nuclear matter. *PoS*, NICXII:125, 2012. doi: 10.22323/1.146.0125.

[75] Nai-Bo Zhang and Bao-An Li. Impact of symmetry energy on sound speed and spinodal decomposition in dense neutron-rich matter. *Eur. Phys. J. A*, 59(4):86, 2023. doi: 10.1140/epja/s10050-023-01010-x.

[76] John Hopkinson. Xiv. magnetic and other physical properties of iron at a high temperature. *Philosophical Transactions of the Royal Society of London.(A.)*, (180):443–465, 1889.

[77] Alfred Actor. Chemical potentials in gauge theories. *Physics Letters B*, 157 (1):53–56, 1985.

[78] H Arthur Weldon. Covariant calculations at finite temperature: The relativistic plasma. *Physical Review D*, 26(6):1394, 1982.

[79] M Loewe, S Mendizabal, and JC Rojas. Skyrme model and isospin chemical potential. *Physics Letters B*, 632(4):512–516, 2006.

[80] Juan Adolfo Ponciano and Norberto Nerio Scoccola. Skyrmions in the presence of isospin chemical potential. *Physics Letters B*, 659(3):551–554, 2008.

Appendix A

On the approximation of the integral (3.3.14)

Equation (3.3.14) is assumed to be independent on p and relates $v = u(2\pi)/p$ to I_0. I_0 is thus expected to be independent on p. To solve this equation one should be able to compute the integral (3.6.1) that we rewrite as

$$\begin{aligned} G(v, I) &= \int_0^v \frac{dx}{\sqrt{1 - e^{-(4x^2+2I)}}} \\ &= v + K(v, I). \end{aligned} \tag{A0.1}$$

where

$$K(v, I) = \int_0^v \Big(\frac{1}{\sqrt{1 - e^{-(4x^2+2I)}}} - 1 \Big) dx. \tag{A0.2}$$

Now, let us consider the function K. Its derivative w.r.t. v is

$$\frac{1}{\sqrt{1 - e^{-(4x^2+2I)}}} - 1 \tag{A0.3}$$

which for positive I and x not too small (already $x \geq 1$ is good) is approximately zero. Therefore, we can approximate (for such values of v) $K(v, I)$ with $K(\infty, v)$. By using

$$(1 - x)^{-b} - 1 = \sum_{n=1}^{\infty} \frac{\Gamma(b + n)}{\Gamma(b)n!} x^n, \tag{A0.4}$$

we get

$$K(\infty, v) = \frac{1}{4} \sum_{n=1}^{\infty} \frac{\Gamma(n+\frac{1}{2})}{\Gamma(\frac{1}{2})n!} \sqrt{\frac{\pi}{n}} e^{-2In}. \tag{A0.5}$$

Now, the Stirling formula gives a good approximation for the Gamma function for arguments larger than 1:

$$\begin{aligned} \Gamma(n+\frac{1}{2}) &\approx (n-\frac{1}{2})^{n-\frac{1}{2}} e^{-n-\frac{1}{2}} \sqrt{2\pi(n-\frac{1}{2})} \\ &\approx n^n e^{-n} \sqrt{2\pi n} (en)^{-\frac{1}{2}} \\ &\approx n! (en)^{-\frac{1}{2}}. \end{aligned} \tag{A0.6}$$

Therefore,

$$\begin{aligned} K(\infty, v) &\approx \frac{1}{4} \sqrt{\frac{\pi}{e}} \sum_{n=1}^{\infty} \frac{1}{n} e^{-2I_0 n} \\ &= -\frac{1}{4} \sqrt{\frac{\pi}{e}} \log\left(1 - e^{-2I_0}\right). \end{aligned} \tag{A0.7}$$

Since $\sqrt{\frac{\pi}{e}} \approx 1$, this justifies (3.6.2). However, the letter seems to become not so good when $I_0 \to 0$ since it diverges. The reason is probably that the above derivation fails when I_0 is very small and v also is small. In this case, $\partial_v K$ fails to be small, and the constant approximation is not good. In this situation, we conveniently rewrite

$$\begin{aligned} G(v, I) &= \frac{1}{4} \int_0^{4v^2} \frac{ds}{\sqrt{s}} \frac{1}{\sqrt{1 - e^{-(s+2I)}}} \\ &= \frac{1}{4} \int_{2I}^{4v^2+2I} \frac{ds}{\sqrt{s-2I}} \frac{1}{\sqrt{1-e^{-s}}}. \end{aligned} \tag{A0.8}$$

Assuming that $I \leq 2v^2 \ll 1$, we can approximate $\sqrt{1-e^{-s}} \approx \sqrt{s}$ so that

$$\begin{aligned} G(v, I) &\approx \frac{1}{4} \int_1^{1+4v^2/I} \frac{dt}{\sqrt{t^2-1}} \\ &= \frac{1}{4} \log\left(1 + \frac{4v^2}{I} + \sqrt{\frac{4v^2}{I}\left(2 + \frac{4v^2}{I}\right)}\right), \end{aligned} \tag{A0.9}$$

which is equivalent to

$$1 + \frac{4v^2}{I} = \cosh(4G(v, I)). \tag{A0.10}$$

Therefore, (3.3.14) gives

$$u \approx p\sqrt{\frac{I_0}{2}}\sinh(4\pi\sqrt{k}L_r). \tag{A0.11}$$

This is expected to be the correct expression when I_0 is very small.
That this is the right behavior when $u \to 0$ can also be inferred from (3.3.14). Indeed, let us set $I_0 \approx 2\lambda\bar{u}^2$, with $\bar{u} := u(2\pi)/p$. Changing the variable τ into $\bar{u}p$, (3.3.14) becomes

$$2\pi\sqrt{k}L_r = \int_0^1 \frac{\bar{u}dx}{\sqrt{1 - \exp(-4\bar{u}^2(x^2 + \lambda^2))}}. \tag{A0.12}$$

Since $x^2 + \lambda^2$ is bounded by $1 + \lambda^2$, for u very small, we can Taylor expand the exponential to first order, getting

$$2\pi\sqrt{k}L_r \approx \frac{1}{2}\int_0^1 \frac{dx}{\sqrt{x^2 + \lambda^2}} = \frac{1}{2}\text{arcsinh}\frac{1}{\lambda}. \tag{A0.13}$$

Therefore,

$$\frac{1}{\lambda} = \sinh(4\pi\sqrt{k}L_r), \tag{A0.14}$$

confirming (A0.11).

Appendix B

The Jacobi theta constant $\theta_3(q)$

The third Jacobi theta function is

$$\vartheta_3(z,q) = \sum_{n\in\mathbb{Z}} q^{n^2} e^{2i\pi z}, \tag{A0.1}$$

convergent for $|q| < 1$. The associated theta constant is

$$\theta_3(q) := \vartheta_3(0,q) = \sum_{n\in\mathbb{Z}} q^{n^2}. \tag{A0.2}$$

Let us introduce the function

$$\Theta(x) := \theta_3\left(e^{-\pi x}\right) = \sum_{n\in\mathbb{Z}} e^{-\pi x n^2}, \qquad \mathrm{Re}(x) > 0. \tag{A0.3}$$

By using the Poisson's resummation formula

$$\sum_{n\in\mathbb{Z}} f(n) = \sum_{m\in\mathbb{Z}} \tilde{f}(m), \tag{A0.4}$$

with

$$\tilde{f}(m) = \int_{-\infty}^{\infty} e^{-2i\pi m t} f(t), \tag{A0.5}$$

to the function Θ, with $f(y) = e^{-\pi x y^2}$ and $\tilde{f}(m) = e^{-\frac{\pi m^2}{x}}/\sqrt{x}$, we get

$$\Theta(1/x) = \sqrt{x}\ \Theta(x). \tag{A0.6}$$

Notice that when $\mathrm{Re}(x) \to +\infty$ then $\Theta(x) \to 1$, so, for $\mathrm{Re}(x) \to 0^+$ we have

$$\Theta(x) = \frac{\Theta(1/x)}{\sqrt{x}} \approx \frac{1}{\sqrt{x}}. \tag{A0.7}$$

Finally, we notice that, for $Re(s) > 0$,

$$\begin{aligned}\int_0^\infty (\Theta(x) - 1) x^{\frac{s}{2}-1} dx =& 2 \sum_{n=1}^{\infty} \int_0^\infty e^{-\pi x n^2} x^{\frac{s}{2}-1} dx \\ =& \frac{2}{\pi^{s/2}} \sum_{n=1}^{\infty} \frac{1}{n^s} \int_0^\infty e^{-z} z^{\frac{s}{2}-1} dz \\ =& \frac{2}{\pi^{s/2}} \Gamma(s/2) \zeta(s).\end{aligned} \tag{A0.8}$$